The Measurement of Cirrus Cloud Structure and Optical Properties with a High Spectral Resolution Lidar and a Volume Imaging Lidar

Edwin W. Eloranta, Principal Investigator
University of Wisconsin
Madison, WI 53706
Tel (608) 262-7327

The University of Wisconsin High Spectral Resolution Lidar (HSRL) and Volume Imaging Lidar (VIL) provide unique, calibrated measurements of cirrus cloud characteristics. This project combined data from these instruments with satellite observations to measure optical propagation in cirrus clouds. This information is required to design systems which must view targets through visible and subvisible cirrus clouds.

The HSRL provides optical depth and scattering cross section measurements which are absolutely calibrated by simultaneous measuring the lidar return from atmospheric gases. Calibrated measurements are achieved without the poorly supported assumptions required to quantify measurements from traditional lidars. The VIL provides high spatial resolution (<60 m) measurements of cirrus structure over spatial domains (>100 km) and with a temporal resolution (<1 min); these capabilities are not available in other lidars.

HSRL measurements were employed to calibrate satellite algorithms used to measure cirrus cloud probability of occurrence, IR emissivity and altitudes. The satellite algorithms are being used in an ongoing program to provide continental and global climatologies of cirrus clouds. Special emphasis was placed on the problem of defining confidence levels for the optical properties measured by the HSRL. While considerable effort had been devoted to the calibration of the HSRL and to the quantification of the errors due to calibration uncertainty, application of the HSRL to cirrus studies raised the potential for an additional error source in comparisons between HSRL and satellite measured emissivities. The satellite measures IR radiances averaged over a footprint several kilometers on a side while the HSRL measures optical depths in a beam approximately 1 m wide and averaged over a time of several minutes. Because of wind oriented structure, and the wide range of spatial scales evident in cirrus clouds, direct comparison of HSRL and satellite measurements showed large sample errors. VIL observations were used to calculate spatial and temporal autocorrelation functions for both visible and subvisible cirrus cloud fields. These observations show that correlation lengths are strongly dependent on direction. Quantitative measurements of the structure of cirrus clouds on spatial scales between 60 m and 100 km were obtained.

Much of the data analyzed in this study was obtained in a pilot experiment which employed a diverse set of remote sensing instruments. The High Spectral Resolution Lidar, the Volume Imaging Lidar, two infrared Fourier transform radiometers, satellite borne radiometers, radiosondes and an all sky imager were used in this campaign.

The results of these investigations are summarized in an attached Masters thesis by Walter Wolf, titled: "Cirrus Cloud Optical and Morphological Variations within a Mesoscale Volume". Additional results are reported in the attached scientific paper: "University of Wisconsin Cirrus Remote Sensing Pilot Experiment" by Ackerman et. al. published in the Bulletin of the American Meteorological Society.

University of Wisconsin Cirrus Remote Sensing Pilot Experiment

Steven A. Ackerman,*
Ed W. Eloranta,**
Chris J. Grund,+
Robert O. Knuteson,++
Henry E. Revercomb,++
William L. Smith,* and
Donald P. Wylie++

Abstract

During the period of 26 October 1989 through 6 December 1989 a unique complement of measurements was made at the University of Wisconsin—Madison to study the radiative properties of cirrus clouds. Simultaneous observations were obtained from a scanning lidar, two interferometers, a high spectral resolution lidar, geostationary and polar orbiting satellites, radiosonde launches, and a whole-sky imager. This paper describes the experiment, the instruments deployed, and, as an example, the data collected during one day of the experiment.

1. Introduction

Uncertainties in model predictions of the climate response to increased greenhouse gas concentrations are largely due to inadequate parameterization of clouds and cloud–climate feedbacks (Cess et al. 1989). Clouds affect climate by exerting a strong influence on radiative heating and cooling distribution within the atmosphere and at the earth's surface. There is an urgent need for measurements that guide and verify for the development of improved methods of treating cloud radiative properties in climate models. This paper describes the University of Wisconsin Cirrus Remote Sensing Pilot Experiment, designed to investigate visible and infrared (IR) optical properties of cirrus clouds and the effects of cloud spatial distribution on the scaling of point measurements to satellite and general circulation model (GCM) grid-scale averages.

Clouds affect the radiative balance of the earth/atmosphere system by reflecting incoming solar radiation and by trapping outgoing longwave radiation. The difference between a clear-sky and a cloudy-sky ra-

diative energy budget is termed cloud radiative forcing. Observations from the Earth Radiation Budget Experiment (ERBE) recently provided estimates of shortwave and longwave cloud radiative forcing (Ramanathan et al. 1989). For the global mean, shortwave cloud radiative forcing is approximately –48 W m^{-2}, while the longwave cloud radiative forcing is approximately 31 W m^{-2}. Thus, the present average cloud cover produces a net radiative cooling of approximately 17 W m^{-2}. In contrast, models suggest that an instantaneous doubling of CO_2 would produce a radiative heating of approximately 4 W m^{-2}. By modificaion of radiative heating distribution, the increased greenhouse gas concentrations in the atmosphere are likely to change planetary circulation patterns and result in a redistribution of moisture and cloudiness. Thus, greenhouse warming trends could produce substantial cloud feedbacks that may serve to moderate or augment the actual global thermal response. Understanding the radiative effects of clouds is therefore crucial to the evaluation of greenhouse gas impacts on climate. In addition to modifying the radiative energy budget at the top of the atmosphere, clouds also modify the radiative heating of the atmosphere and surface.

Cirrus clouds are important modulators of earth's radiative balance because of their large areal extent, seasonal persistence, and typically high-altitude location. These clouds have only recently been subject to detailed measurements (*Mon. Wea. Rev.,* **118,** 2259–2248). Climate models suggest that cirrus may produce a positive or a negative feedback response to global warming depending on cloud optical depth, altitude, and particle size distribution (Roeckner et al. 1987; Stephens et al. 1990). In order to address some specific issues concerning the remote sensing and radiative parameterizations of cirrus clouds, simultaneous observations were made at the University of Wisconsin—Madison during the Cirrus Remote Sensing Pilot Experiment (CRSPE). CRSPE employed a unique complement of instruments in conjunction with satellite and National Weather Service meteorological observations. Section 2 describes CRSPE science

*Cooperative Institute for Meteorological Satellite Studies, Madison Wisconsin.
+Space Science and Engineering Center, Madison, Wisconsin.
**Department of Meteorology, University of Wisconsin, Madison, WI 53706
++NOAA/ERL Wave Propagation Laboratory, Boulder, Colorado

objectives and section 3 gives a brief description of instruments deployed. Section 4 presents a qualitative description of how the data support the scientific objectives by presenting examples of data collected on 1 December 1989.

2. Science objectives

Development of cirrus radiative parameterizations for model applications is particularly challenging for several reasons. Cirrus are composed largely of ice crystals exhibiting a wide range of shapes, sizes, and orientations. Cirrus are spatially inhomogeneous and often exhibit coherent structures in all size regimes, from tens of meters to the synoptic scale. While

Ultimately, global measurement and monitoring of cirrus cloud cover and radiative properties are necessary. Current satellite-borne passive instrumentation can provide the needed global coverage, but cloud property retrieval techniques require verification and calibration.

accurate and detailed measurements of the radiative, microphysical, and morphological properties of cirrus are needed, cloud variability and high cloud altitudes hamper in situ particle and radiation measurements.

Ultimately, global measurement and monitoring of cirrus cloud cover and radiative properties are necessary. Current satellite-borne passive instrumentation can provide the needed global coverage, but cloud property retrieval techniques require verification and calibration.

Interpretation of satellite radiometric measurements is often based on simplified model calculations or ground-based point observations. Scaling point measurements or theoretical calculations of cloud optical properties to satellite pixel-sized areal averages, or to GCM grid volumes, are not trivial due to spatial and temporal inhomogeneity of cirrus. To improve the radiation parameterization in global climate models using information from a densely instrumented site, an estimation of radiation fields averaged over GCM grid boxes must be produced from the point measurements. CRSPE was designed to provide a database suitable for addressing the problems of extrapolating point measurements to the GCM scales. Specific science objectives are listed below.

1) Characterization of the effect of horizontal and vertical cloud inhomogeneities on satellite- and ground-based observations. The ground-based high spectral resolution lidar and the interferometers (see next section) will provide "point" observations of the cirrus cloud with a field of view (FOV) of less than 1 km. The combination of scanning lidar and satellite data will be used to describe the horizontal and vertical structure of the cloud on the mesoscale, the portion of the cloud that passed over the central site, and the changes in the clouds during the period of the observations.

2) Parameterization of visible and infrared cirrus optical properties. Cloud radiative parameterizations will be developed from the measured visible properties and the infrared emissivities derived from the ground- and satellite-based observations from a variety of cirrus cloud types. The effects of cloud inhomogeneities on these relationships will be investigated.

3) Verification of satellite cloud retrieval methods. Satellite- and ground-based cloud detection schemes will be compared and verified with lidar observations. Cloud optical properties derived from satellite and ground-based radiometric observations will be cross validated.

4) Statistical description of cirrus spatial scales. Autocorrelations of lidar backscatter will be used to determine statistics of cirrus cloud spatial characteristics.

5) Database for comparisons with radiative transfer models. The interferometers provide accurate measurements of downward infrared radiance spectra under clear-sky conditions for comparison with radiative transfer model calculations. Pristine skies are not observed in nature and the lidars therefore play a vital role in detecting and locating aerosol and subvisible cirrus. Radiosonde observations provide in situ measurements necessary to define the detailed atmospheric temperature and moisture structure required for radiative calculations.

3. The field experiment

The experiment was conducted over south-central Wisconsin from 1 November to 6 December 1989. This was also the location of the FIRE–Cirrus IFO in October 1986 (Cox et al. 1987; Starr 1987). Ground- and satellite-based observations of clear skies and various cirrus cloud systems were made during this one-month period. At the central site, located on the University of Wisconsin—Madison campus, four primary instrument systems operated: two calibrated interferometers with a spectral resolution of approxi-

mately 1 cm^{-1}, the high spectral resolution lidar, a Scripps Whole-Sky Imager (WSI), and an NCAR CLASS radiosonde system. Located 24 km west of the central site, the volume imaging lidar (VIL) was operated with a clear line of sight over the central site. Satellite-based observations over the region were captured in real time by the McIDAS system (Suomi et al. 1983), located at the central site. These instruments are discussed in detail below.

High Spectral Resolution Lidar (HSRL) provides calibrated measurements of the vertical profile of the cirrus backscatter cross section, optical depth, and backscatter phase function at a wavelength of 0.532 m. Using a two-channel multietalon receiver, the HSRL spectrally separates molecular backscatter from cloud particle and aerosol backscatter. The separation is possible because the thermal motions of molecules Doppler broadens the molecular backscatter spectrum, while the Brownian motions of particles produce insignificant broadening of the particle backscatter spectrum (Grund and Eloranta 1991). HSRL observations are also used for diagnosing cloud-base altitude, geometric thickness (for optically thin cloud), and vertical distribution.

High-Spectral Resolution Interferometer Sounder (HIS). Two Michelson interferometers were located at the ground site. The first was the aircraft version that was flown on the NASA ER-2 during FIRE I (Revercomb 1987). The second was based on a Bomem M-120 spectrometer that was being developed for use in the Department of Energy's Atmospheric Radiation Measurement (ARM) Program. A motor-driven mirror directs infrared energy into the M-120 from one of three sources: an ambient blackbody cavity, a cold blackbody source, or the atmosphere. The blackbody views are used to remove the effect of instrument emission from sky radiance through the use of a standard linear calibration. The demonstrated rms noise is approximately 0.1% of ambient temperature. The interferometers provide high spectral resolution (on the order of 1 cm^{-1}) observations of cirrus clouds in the 3.5–20-μm spectral band. The observed spectra allow detailed comparisons with line-by-line radiative transfer models such as FASCOD (Clough et al. 1988; Revercomb et al. 1989). Observations also provide variability estimates of the infrared spectral emissivity of clouds. Atmospheric temperature and moisture profiles are also retrieved from these observations.

Volume Imaging Lidar (VIL) produces 3D reconstructions of cirrus cloud backscatter by assembling successive 2D crosswind scans. The VIL scans 120-km-wide segments of cirrus at a resolution of approximately 60 m in 20 s. During the experiment, one scan plane was oriented above the central site, while a second scan plane was oriented perpendicular to the mean wind direction or perpendicular to the central site scan plane. During CRSPE, the VIL scan over the central site provided a 2D view of cirrus clouds with 100-m resolution. Time composites of the VIL crosswind scans provide the 3D structure of the cloud, thus describing vertical and horizontal variations of the cirrus cloud backscatter. The VIL observations provide a means for investigating effects of subpixel-scale variability and cloud vertical distribution on the retrieval of cloud height and optical properties from current meteorological satellite sensors and ground-based instruments.

Satellite observations include multispectral data from the polar-orbiting NOAA AVHRR (both GAC and HRPT), HIRS/2 and MSU, and *GOES-7* VISSR and VAS data captured in real time by the McIDAS system. These radiometers produce multispectral images of the earth's upwelling radiance with resolutions of 1–8 km depending on wavelength and instrument. The meteorological satellites observe clouds on the scale of tens to thousands of kilometers, thus bridging the gap between the scale of site observations and the regional scales used in GCMs. Satellite visible and infrared observations can be used for diagnosing large-scale geometric and radiative cloud structure.

NCAR Cross-chain Loran Atmospheric Sounding System (CLASS) produces accurate in situ radiosonde determination of atmospheric profiles of temperature, water vapor, and wind speed and direction. A unique feature of the CLASS is that it uses the Loran-C navigation system to determine accurate positions from which to calculate wind speed and direction as a function of altitude during the balloon ascents. The CLASS soundings of temperature and moisture represent point measurements along the balloon flight path but possess the vertical resolution and accuracy required for comparing infrared radiance observations with theoretical calculations from atmospheric radiation models. The temperature and moisture profiles provide thermodynamic properties of the cloud and the surrounding atmosphere as well as density profiles to calibrate HSRL optical depths. Wind speed and direction profiles from the CLASS are used to construct the 3D images from VIL scans.

SCRIPPS Whole-Sky Imager (WSI) generates a time record of sky conditions through a 170° FOV fisheye CCD camera. Regularly spaced digital "snapshots" through red, blue, and neutral density filters are provided to facilitate cloud detection and accommodate varying light conditions (Johnson et al. 1989).

National Weather Service surface and radiosonde observations. These routine observations are available through McIDAS and describe the synoptic condition associated with the cirrus clouds.
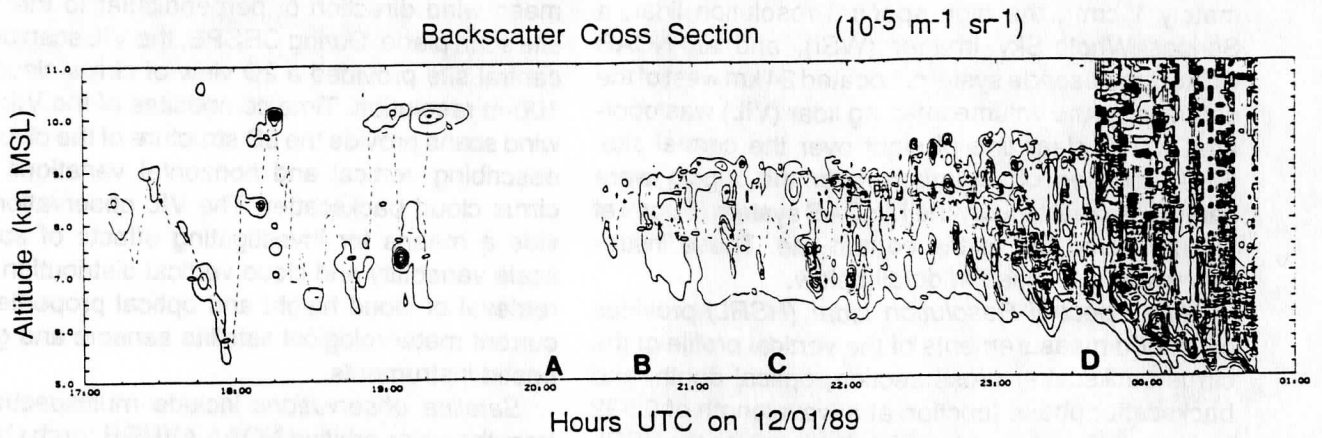
Backscatter Cross Section $(10^{-5}\ m^{-1}\ sr^{-1})$

FIG. 1. HSRL-observed backscatter cross section as a function of altitude on 1 December 1989.

4. Case study (1 December 1989)

This section illustrates types of data collected during CRSPE from examples collected on 1 December 1989. The two interferometers (results are shown only for the Bomem M-120) collected data from approximately 1400 to 2400 UTC; the HSRL operated from 1345 to 0110 UTC and the VIL from 1800 to 2330 UTC. Four CLASS sondes were launched and the WSI imaged the sky throughout the day. The *NOAA-11* satellite flew over Madison at approximately 1350 UTC. Examples of data products are first presented separately for each instrument; an integrated example of the data is presented at the end of the section.

Figure 1 depicts the HSRL-measured backscatter cross section as a function of altitude for eight hours on 1 December 1989. Contour intervals are 2×10^{-5} $m^{-1}str^{-1}$. The dashed line marks the optical midcloud altitude (midpoint in optical depth). Between approximately 1930 and 2015 UTC, the HSRL backscatter measurements indicate that the upper troposphere is essentially free of cirrus and aerosol. No clouds were observed visually during this time. Prior to 1930 UTC, the HSRL backscatter cross-section measurements indicate the presence of a cirrus cloud or aerosol layers with backscatter cross sections ranging from approximately 1×10^{-7} to 12×10^{-5} $m^{-1}str^{-1}$, and optical midcloud altitude ranging from 5.5 to 10 km. Visual observations of sky conditions during this period indicated the presence of thin cirrus fibratus. These visual cirrus are associated with regions of high backscatter cross section at approximately 1815 and 1910 UTC. After approximately 2020 UTC, the HSRL backscatter cross-section measurements coincide with a visually observed cirrus cloud layer. The HSRL-measured cloud top is above 9 km with cloud base at approximately 6.5 km, which begins to descend around 2330

UTC. As the cloud base descends, the cloud optical depth increases so that at approximately 2340 UTC the HSRL lidar beam cannot penetrate through the cloud (optical depth greater than 2.7, indicated by vertical hatching).

The temperature and moisture profiles measured by the CLASS are depicted in Fig. 2, for launch times of 1445, 1800, 2124, and 2356 UTC. Between 1445 and 2124 there is a general warming trend below 800 mb, while a cooling trend exists between 2124 and 2356 UTC. During the period 1445 to 1800 UTC, a significant moistening of the atmospheric layer between 300 and 500 mb occurs. The existence of a
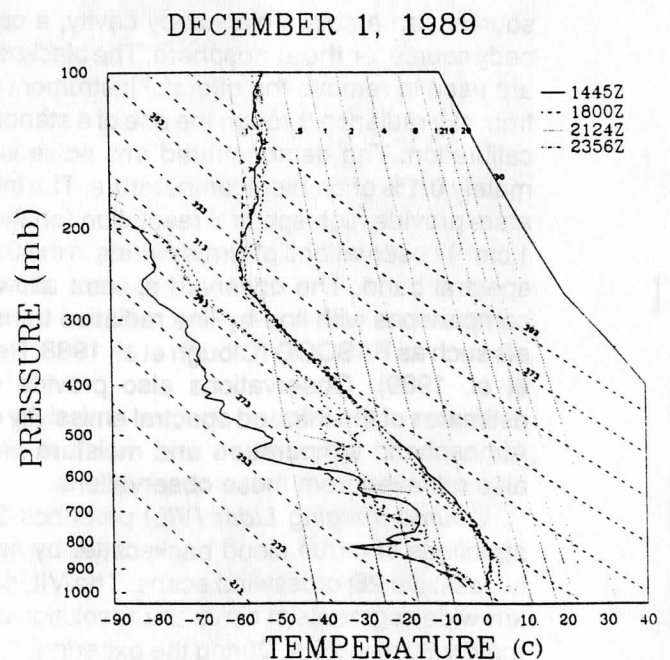
DECEMBER 1, 1989

FIG. 2. Temperature and moisture profiles measured by the CLASS at four time periods.

cirrus cloud is suggested from an increase in the dewpoint at approximately 5.6 km (497 mb) at 1800 UTC, 7.3 km (390 mb) at 2124 UTC, and 5.9 km (475 mb) at 2356 UTC. The radiosonde cloud-base altitudes are higher than indicated by the lidar due in part to the time response lag of the hygristor. Similarly, the cloud-top altitude inferred from the radiosonde temperature and moisture profile is higher than indicated by the lidar backscatter signal. Some difference in cloud-top height may also be due to the CLASS sonde sampling a different portion of the atmosphere than the lidar, as well as measurement errors associated with the low humidities of the upper troposphere (Finger and Schmidlin 1991; Elliott and Gaffen 1991).

An example of the observed infrared spectra is depicted in Fig. 3 in terms of brightness temperature as a function of wavenumber. These spectra were collected over a 5-min sampling period at 2006, 2043, 2138, and 2337 UTC (these times are depicted on the HSRL backscatter cross-section time series of Fig. 1). Several gaseous absorption bands are denoted in Fig. 3. The 620–700-cm^{-1} carbon dioxide band is a strong absorption band that indicates changes is surface air temperature. This band has been used to retrieve low-level temperature inversions (Smith et al. 1990). The 1040-cm^{-1} (9.6-μm) ozone band is clearly evident in the clear-sky spectra, but as the cloud opacity increases the signature weakens as the emission from stratospheric ozone is attenuated by the cloud. Several water vapor absorption bands are clearly evident in the 800–1200-cm^{-1} (8–12-μm) window region. Figure 4 is an enlargement of Fig. 3 for the 800–1000-cm^{-1} region, a common spectral interval covered by narrowband radiometers. Techniques for retrieving cirrus cloud properties from narrowband radiometer observations must remove the effects of these absorption lines by using coincident atmospheric temperature and moisture profiles along with model calculations. An advantage of highspectral resolution observations is that analysis can be done between the absorption lines; however, absorption due to the water vapor continuum must still be accounted for.

The HSRL and CLASS observations are point measurements of the atmospheric vertical structure. While time series analyses give some indication of atmospheric variability, scene variability within the HSRL and the interferometer field of view is unknown. The horizontal and vertical variability of the cirrus cloud observed at 2153 UTC is depicted from the VIL observations in Fig. 5. The top portion of the figure depicts the scan perpendicular to the wind direction and the bottom portion is for the scan in the direction of the ground site. The location of the central site (24 km from the VIL) is depicted in the lower portion of the figure. The VIL scans clearly indicate the heteroge-
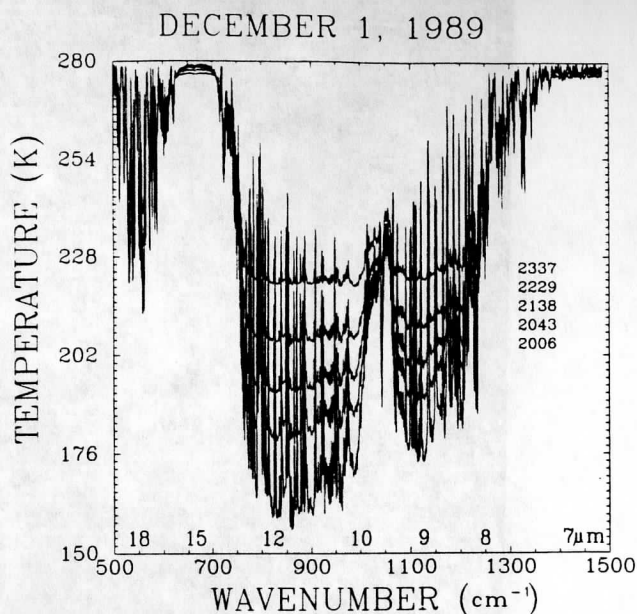

FIG. 3. Five BOMEM-120-observed infrared spectra, in terms of brightness temperature, for the 500–1500 cm^{-1} (wavelength in microns is also shown). Cloud cover increases during this time period.
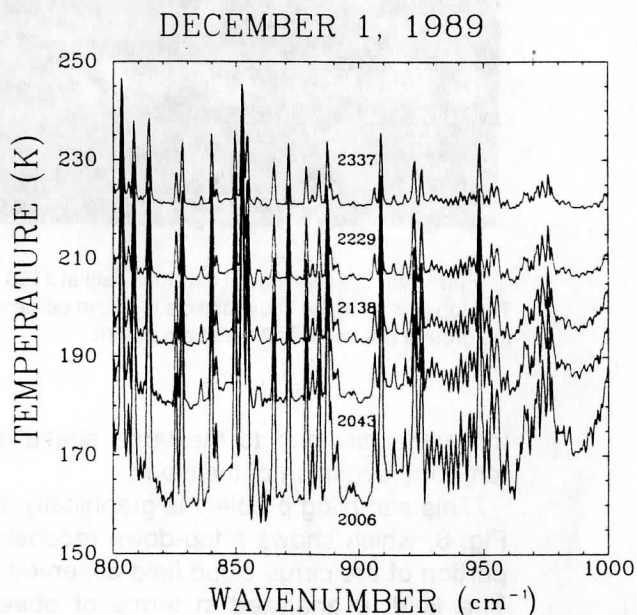

FIG. 4. Enlargement of the 800–1000-cm^{-1} spectral region for the five spectra depicted in Fig. 3.

neous nature of cirrus cloud, which appears to consist of several individual layers. The VIL data also indicate that ice crystals are falling out of the cloud base at approximately 6.5 km and evaporating. Images from the VIL suggest that single point measurements (e.g., HSRL or M-120) of mean quantities may exhibit large fluctuations due to the heterogeneous nature of the cloud. Temporal averaging of the data may not reduce
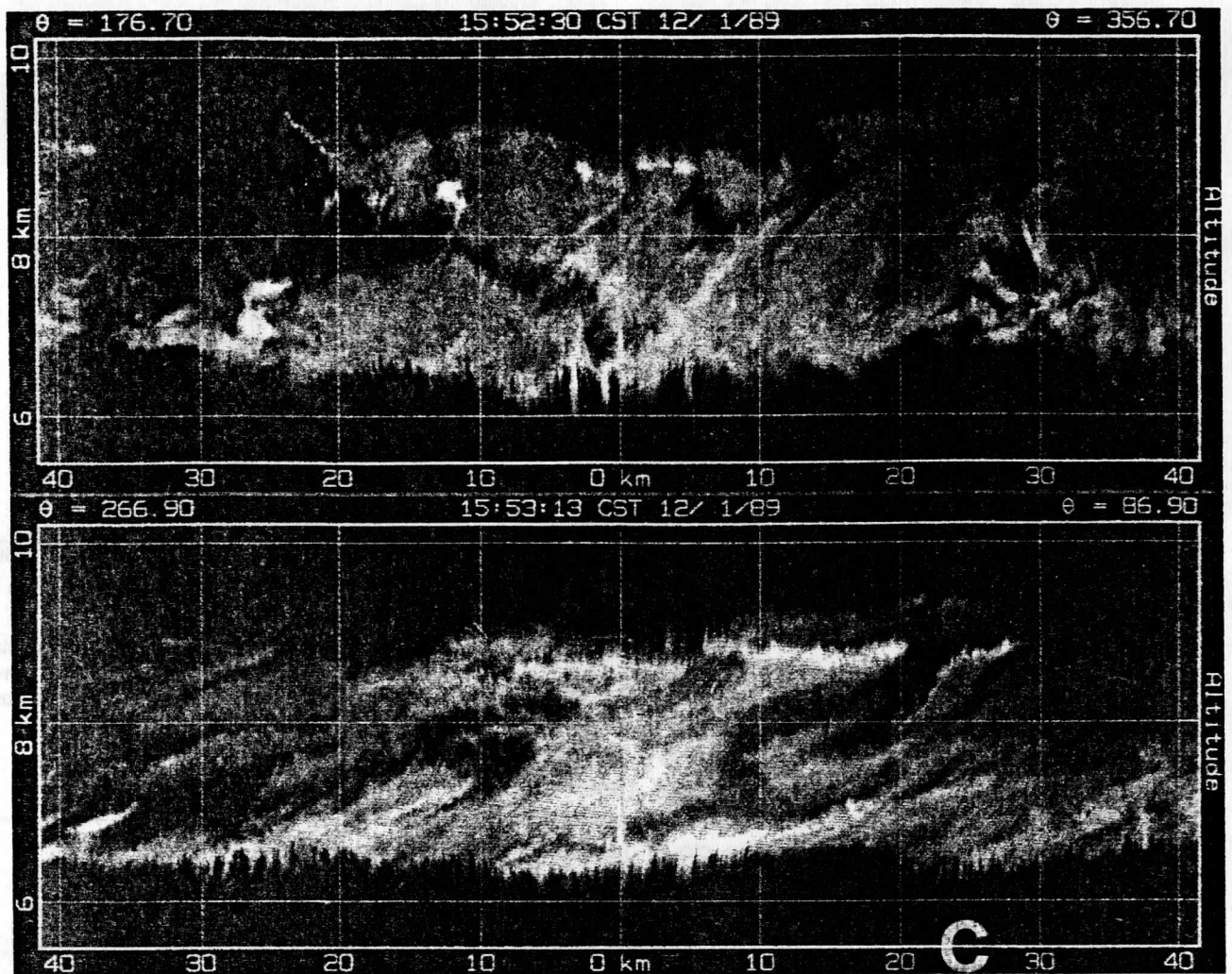
FIG. 5. VIL observations of the cloud field at 2153 UTC (1553 CST). The ordinate is altitude and the abscissa is distance from the VIL. The top portion of the figure depicts the scan perpendicular to the wind direction and the bottom portion is for the scan in the direction of the ground site, located 24 km from the VIL.

this variability due to the large spatial scales and temporal evolution of the cloud.

This sampling problem is graphically illustrated in Fig. 6, which shows a top-down reconstruction of a portion of the cirrus cloud field observed by the VIL. The field is analyzed in terms of observed cloud fraction in two separate 1-h periods, as would be observed by vertically oriented point sensors spaced approximately 10 km apart. This image presents north–south distance on the vertical axis and observation time along the sloping lines. The rectangular grid squares represent 50 km each. In the north–south direction, these are actual measured distances. The distances on the x axis have been computed from wind velocities measured by the CLASS radiosonde. The lidar data used to generate this image consists of approximately 120 north–south lidar scans, each composed of approximately 900 profiles each containing

1024 data points. A signal threshold is chosen and a surface is drawn such that backscatter regions larger than the cloud threshold are enclosed by the surface. The cloud cover figures are shown for 12 different observation points placed at 10-km intervals along a north–south line. The cloud cover percentages on the left of the figure are for times between 14:30 and 15:30 CST and the percentages on the right for the times between 13:30 and 14:30 CST. Notice that even for 1-h averages, cloud cover percentages are highly variable between closely spaced observations points. For the period 13:30 to 14:30, cloud cover varies between 36% and 87%, while in the next hour cloud cover varies spatially between 0% and 73%. These variations make point measurements difficult to compare with area averages over a satellite pixel. Coincident HSRL, interferometer, and VIL data allow the capability to characterize the effect of the cloud horizontal and

vertical inhomogeneities on single, time-averaged point measurements.

Satellite observations depict large-scale structure of the cirrus cloud system. Figure 7 is an example of a GOES visible and infrared image at approximately 2100 UTC. Also shown in Fig. 7 is the VIL scan pattern (cross) as well as the central site location (box). Time series analysis of the GOES imagery, at half-hour time intervals, indicates that the cloud system in northern Wisconsin moves to the south and southeast and arrives over Madison sometime between 2000 and 2100 UTC.

While it is not the intent of this paper to present the type of analysis required to achieve the objectives outlined in section 2, it is, however, useful to present an integrated picture of the various datasets. The first question to address is the capability of the VIL to simulate cloud structure within the field of view (FOV) of the single-point measurements. This is crucial to our first science objective and is best demonstrated by comparing a time series of the observed HSRL backscatter with a simulated time series generated by the VIL observation over and within the HSRL FOV. This comparison is depicted in the top two panels of Fig. 8. There is an excellent correlation

FIG. 6. Top-down view of cirrus clouds constructed from VIL observations. This image presents north–south distance on the vertical axis and observation time along the sloping lines. The rectangular grid squares represent 50 km each. Presented on this figure are the percentages of the time an observer would see cirrus cloud cover at zenith during two separate 1-h time intervals. Cloud cover figures are shown for 12 different observations points placed at 10-km intervals along a north–south line. Cloud cover percentages on the left of the figure are for times between 14:30 and 15:30 CST and the percentages on the right for the times between 13:30 and 14:30 CST.

between the VIL-simulated and HSRL time series. The capability of the VIL to simulate the HSRL signals demonstrates that the VIL can be used to characterize temporal and spatial variations within the FOV of the point observations. It also lends confidence in using
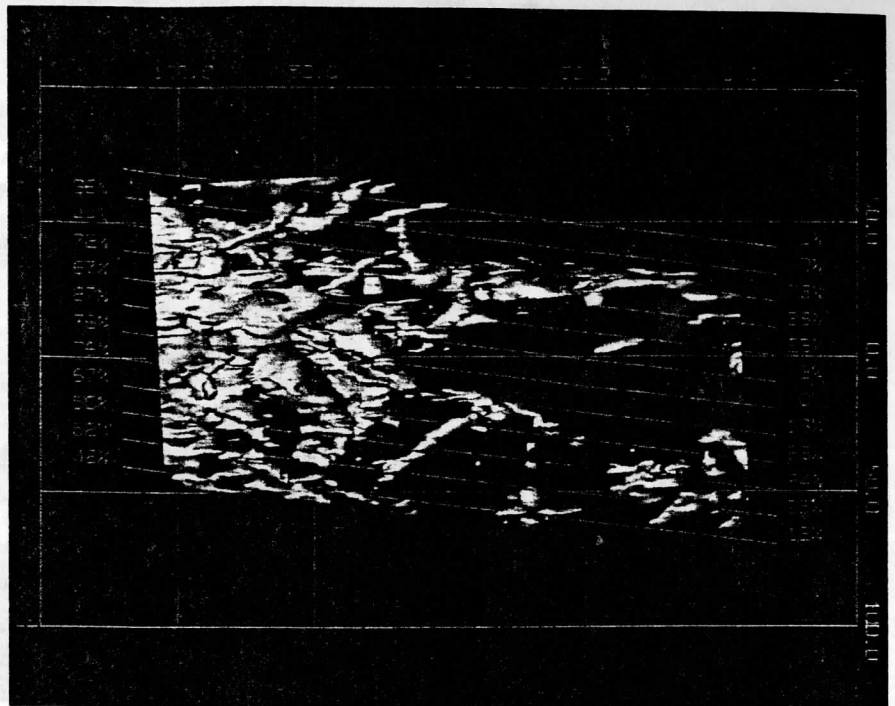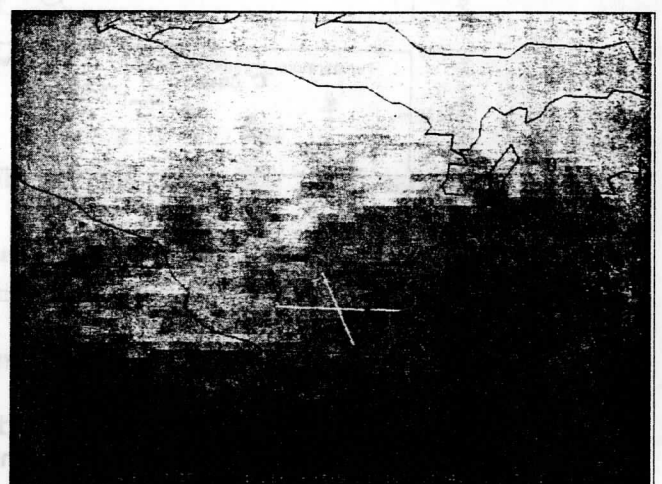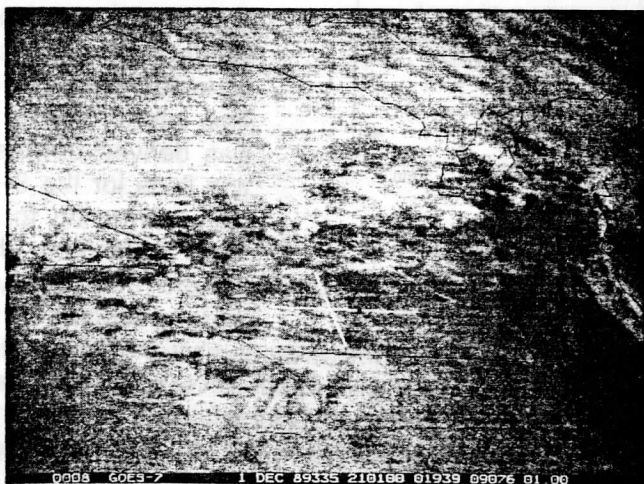

FIG. 7. GOES imagery at 1900 UTC. Also shown is the VIL scan pattern as well as the central site location.
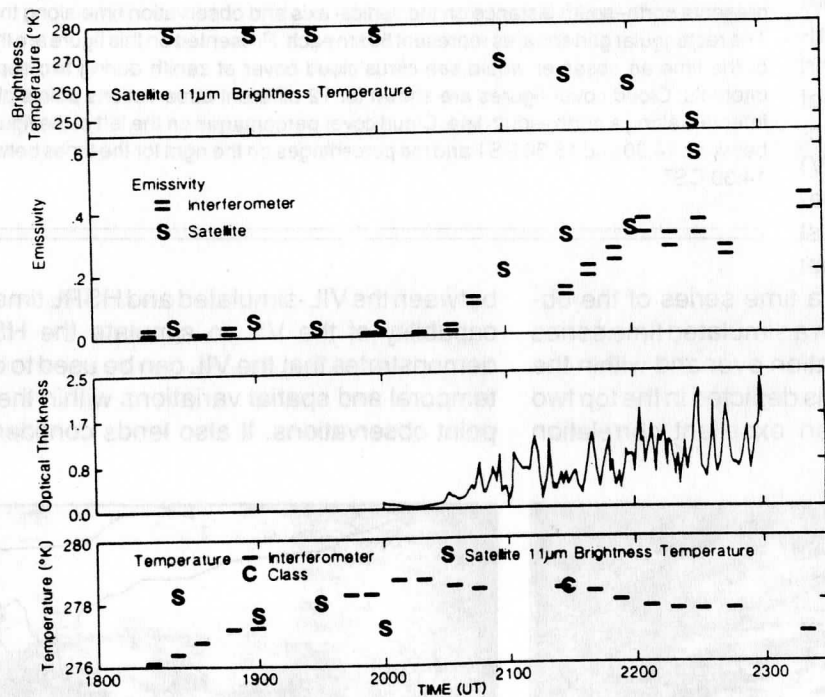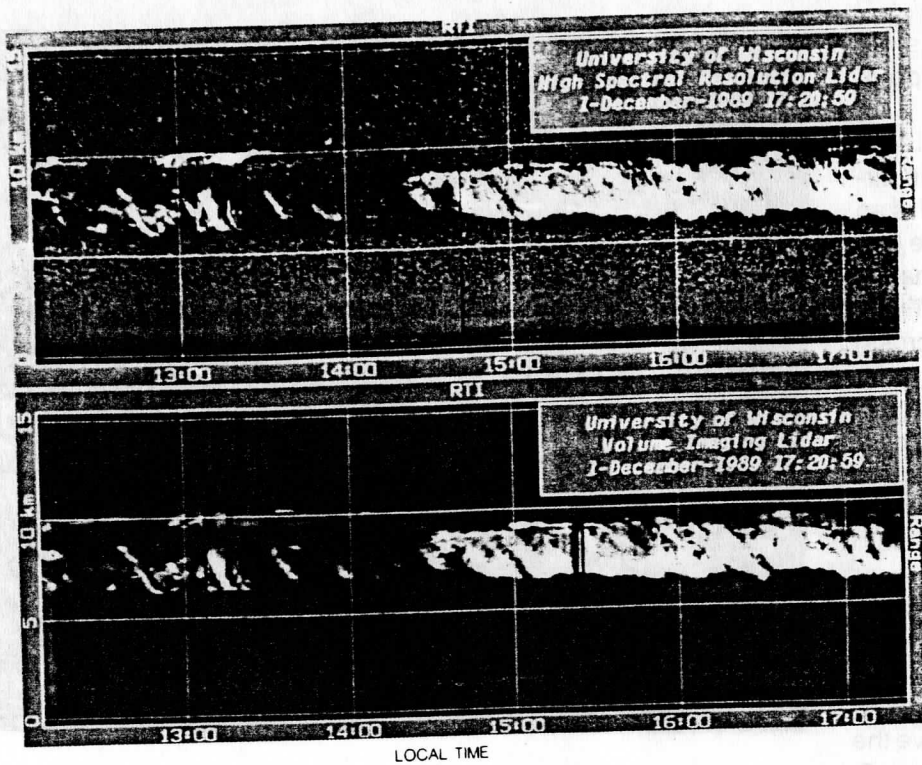
FIG. 8. An integrated depiction of the various datasets. See text for details.

the VIL for statistical descriptions of cirrus spatial scales (objective 4).

Analysis of GOES data is best visualized by animating the satellite imagery. Depicted in the third panel of Fig. 8 is a time series of GOES VISSR 11-μm brightness temperature for the pixel nearest to the central

site. As seen in the satellite animation, decrease in brightness temperature beyond 2030 UTC is due to development of a thick cirrus deck over the central site. The cloud system appeared to be moving from the north-northwest, and therefore its movement was nearly perpendicular to the VIL scan over the central site. The satellite-observed brightness temperature decreases as the observed energy becomes more characteristic of cloud emission rather than surface emission. This can be manifested by an increase in cloud areal coverage within the 8-km satellite footprint, an increase in the cloud opacity, or a combination of both. Again, scanning lidar observations will be used to quantify spatial variability within the satellite pixel FOV and its effect on the satellite retrieval algorithm (objective 3).

Emissivity is often used to parameterize the infrared radiative properties of clouds (objective 2) and is defined as cloud radiance normalized by equivalent radiance of a blackbody at the cloud temperature. The satellite-derived cloud emissivity, derived after the method presented by Wylie and Menzel (1989), is denoted by the "S's" in the fourth panel of Fig. 8. Also shown in this panel are emissivities derived from ground-based interferometer measurements, denoted by two horizontal lines. The interferometer emissivity was derived between absorption lines for the 8–12-μm region, correcting for the water vapor continuum. The spectral variation of emissivity across this band is denoted by the vertical spacing of the two bars, while the length of the two bars denotes the time period over which the measurements were averaged. Comparison of these line widths with the lidar images at the top of the figure gives some indication of the temporal variability of the scene. Spectral variability in emissivity is on the order of 10%–

15% of the 8–12-μm band mean emissivity. Differences between satellite-derived emissivity and spectral emissivity are due to the different FOV of the two observations.

In parameterizing radiative properties of clouds, it is important to properly couple the shortwave and longwave properties. One such method is a functional relationship between visible optical thickness and window infrared emissivity. A time series plot of the HSRL-observed visible optical thickness is shown in panel 5 of Fig. 8, for 2-min averages. This relationship between the HSRL visible optical thickness and the infrared emissivity will be the basis of the parameterization discussed in objective 2.

The final panel of Fig. 8 depicts the time series of HIS-observed equivalent blackbody temperatures in the 620–700-cm^{-1} spectral band and is representative of the air temperature in the vicinity of the instrument. The "C" represents the corresponding CLASS measurement. The satellite observed 11-μm brightness temperature is also plotted for reference. The agreement between the CLASS and the 620–700-cm^{-1} spectral channel temperatures indicates that this channel can be used to monitor low-level atmospheric temperature changes between CLASS sonde launches. This is important for determining the effects of the lower atmosphere on deriving cloud radiative properties. The coincident CLASS, lidar, and interferometer observations will also be used to improve radiation calculations under clear- and cloudy-sky conditions (objective 5).

5. Summary

An experiment to improve radiative parameterizations of clear and cloudy atmospheres was carried out at the University of Wisconsin in November and December 1989. This experiment consisted of simultaneous observations from a unique compliment of instruments, designed to address important issues concerning the parameterization of radiation in global climate models. This paper presented an example of data collected during one day of the experiment. It is clear that a larger dataset needs to be obtained before all science objectives can be fully met. In addition to the observations from CRSPE, these instruments participated in the cirrus FIRE II experiment in November 1992 in Kansas.

References

Cess, R. D., G. L. Potter, J. -P Blanchet, G. J. Boer, S. J. Ghan, et al., 1989: Interpretation of cloud–climate feedback as produced by 14 atmospheric general circulation models. *Science,* **245,** 513–516.

Clough, S. A., R. D. Worsham, W. L. Smith, H. E. Revercomb, R. O. Knuteson, H. W. Woolf, G. P. Anderson, B. L. Hoke, and F. X. Kneizys, 1988: Validation of FASCOD calculations with HIS spectral radiance measurements. *International Radiation Symposium.* Lille, France, 376–379.

Cox, S. K, D. S. McDougal, D. A. Randall, and R. A. Schiffer, 1987: FIRE—The First ISCCP Regional Experiment. *Bull. Amer. Meteor. Soc.,* **68,** 114–118.

Elliot, W. P., and D. J. Gaffen, 1991: On the utility of radiosonde humidity archives for climate studies. *Bull. Amer. Meteor. Soc.,* **72,** 1507–1520.

Finger, F. G., and F. J. Schmidlin, 1991: Upper-Air Measurements and Instrumentation Workshop—Meeting review. *Bull. Amer. Meteor. Soc.,* **72,** 50–55.

Grund, C. J., and E. W. Eloranta, 1991: The University of Wisconsin High Spectral Resolution Lidar. *Optical Engin.,* **30,** 6–12.

Johnson, R. W., W. S. Hering, and J. E. Shields, 1989: Automated visibility and cloud cover measurements with a solid state imaging system. Final Report GL-TR-89-0051. Geophysics Laboratory, Hanscom AFB, SIO Ref. 89-7 MPL-U-26/89.

Ramanathan, V., R. D. Cess, E. F. Harrison, P. Minnis, B. R. Barkstrom, E. Ahmad, and D. Hartmann, 1989: Cloud-radiative forcing and climate: Results from the Earth Radiation Budget Experiment. *Science,* **243,** 57–63.

Revercomb, H. E., J. Buijs, H. B. Howell, D. D. LaPorte, W. L. Smith, and L. A. Sromovsky, 1988: Radiometric calibration of IR Fourier Transform Spectrometers: Solution to a problem with the High-spectral resolution Interferometer Sounder. *Appl. Optics,* **27,** 3210–3218.

——, W. L. Smith, L. A. Sromovsky, R. O. Knuteson, H. M. Woolf, and H. B. Howell, 1989: Comparisons of FASCOD spectra with HIS observations. *Proc. of the AFGL Annual Review Conference on Atmospheric Transmission Models.* Geophysics Laboratory, Hanscom AFB, 537–573.

Roeckner, E., U. Schlese, J. Biercampound, and P. Loewe, 1987: Cloud optical depth feedbacks and climate modeling. *Nature,* **329,** 138–149.

Smith, W. L., H. E. Revercomb, H. B. Howell, H. M. Woolf, R. O. Knuteson, et al., 1990: GAPEX: A ground-based atmospheric Profiling Experiement, Bull. Amer. Meteor. Soc., 71, 310–318.

Starr, D. O'C., 1987: A cirrus-cloud experiment: Intensive field observations planned for FIRE. *Bull. Amer. Meteor. Soc.,* **68,** 119–124.

Stephens, G. L., S. C. Tsay, P. W. Stackhouse, and P. J. Flatau, 1990: The relevance of the microphysical and radiative properties of cirrus clouds to climate and climatic feedback. *J. Atmos. Sci.,* **47,** 1742–1753.

Suomi, V. E., R. J. Fox, S. S. Limaye, and W. L. Smith, 1983: McIDAS III, A modern interactive data analysis facility. *J. Clim. Appl. Meteor.,* **22,** 766–778.

Wylie, D. P., and W. P. Menzel, 1989: Two years of cloud cover statistics using VAS. *J. Climate Appl. Meteor.,* **2,** 380–392.

CIRRUS CLOUD OPTICAL AND MORPHOLOGICAL VARIATIONS WITHIN A MESOSCALE VOLUME

By

Walter W. Wolf

A THESIS SUBMITTED IN PARTIAL FULFILLMENT OF THE
REQUIREMENTS FOR THE DEGREE OF

Master of Science
(Atmospheric and Oceanic Sciences)

at the

UNIVERSITY OF WISCONSIN – MADISON

1994

Approved by: _____

Roland Stull

Professor, Atmospheric and Oceanic Sciences

Approved by: _____

Edwin Eloranta

Senior Scientist, Atmospheric and Oceanic Sciences

Date: _____ 16 Dec 93 _____

Abstract

Cirrus cloud optical and structural properties were measured above southern Wisconsin in two time segments between 18:07 and 21:20 GMT on December 1, 1989. These clouds were measured using the University of Wisconsin–Madison Volume Imaging Lidar (VIL), the University of Wisconsin–Madison High Spectral Resolution Lidar (HSRL), and the VISSR Atmospheric Sounder (VAS) situated on GOES. The VIL imaged the cirrus cloud structure within a mesoscale volume and detected cirrus cloud cover percentages of 81.5% and 76.8% for the two time periods. A series of RTIs were created from the VIL cirrus scans to simulate many vertically pointing lidars situated across the wind. The cloud cover percentages for the individual RTIs ranged from 54.7% to 100%. The variation of the cirrus cloud features across the wind indicate the sampling errors associated with point measurements when they are used to describe the mesoscale cirrus cloud structure. The average cloud length along the wind was 130 km while the average cloud length across the wind was 14 km. The distance between clouds was 273 km along the wind and 24 km across the wind.

A new technique was used to calculate the cirrus cloud visible aerosol backscatter cross sections for a single channel elastic backscatter lidar. Cirrus clouds were viewed simultaneously by the VIL and the HSRL. This allowed the HSRL aerosol backscatter cross sections to be directly compared to the VIL single channel backscattered signal. This first attempt resulted in an adequate calibration. The calibration was extended to all the cirrus clouds in the mesoscale volume imaged by the VIL. This enabled the VIL backscattered signal to be converted into aerosol backscatter cross sections at a resolution of 2 to 3 km along the wind direction and a 60 m resolution both horizontally across the wind and in the vertical. Usage of a constant aerosol backscatter phase function (0.0499 sr^{-1}) enabled the calculation of extinction cross sections at each data point in the VIL observed mesoscale volume. This allowed for the cirrus cloud visible scattering optical depths to be calculated throughout the imaged volume. The VIL volume

was viewed from the position of the GOES to directly compare the VIL visible scattering optical depths to the VAS infrared absorption optical depths. The resulting ratio of the visible scattering optical depths to the infrared absorption optical depths was approximately 2:1.

Acknowledgments

I would like to thank Dr. Edwin W. Eloranta for his patience and guidance throughout this ordeal. What can I say Ed. You believed in me when perhaps I didn't believe in myself. Your comments, criticisms, and 'suggestions' helped to bring this work together. You have shown me the correct way to do science. (By the way, I hope this section does not need any corrections.)

I would like to thank Dan Forrest whose vast computer knowledge helped me out of many situations. His ability to see the root of a problem, or even the obvious which I often missed, has kept me on the right track. I guess that is what friends are for.

Antti and Paivi Piironen, without you two this thesis would not have been completed. While putting this work together, it was the small details which caused the most trouble. Antti, thanks for all of the programs; Paivi thanks for keeping my facts straight.

Dr. Donald Wylie, thanks for your cooperation with the satellite data. There is still a lot of work to be done.

I would like to thank Professors Steve Ackerman, William Smith, and Roland Stull for reading this work and for their helpful comments and suggestions.

I would also like to thank my parents, Joseph and Carole Wolf, because they started all of this many years ago. Thanks for the love and support throughout the years.

Last, but certainly not least, I would like to sincerely thank my wife Michelle for all the love and support she has given me over the years. She was always there when I started questioning whether it was all worth it. Her devotion and unselfishness made the extra hours a little easier to handle. Maybe I will be home at a reasonable hour now ... maybe.

Contents

1   Introduction

Cirrus clouds have a direct impact on the radiation balance of the Earth-Atmosphere system. These clouds reflect a portion of the incoming solar radiation and partially absorb the outgoing infrared radiation. The reflection of the incoming solar radiation reduces the energy added to the system. The partial absorption of the outgoing infrared radiation reduces the energy lost to space. This occurs because the cirrus clouds absorb the upwelling infrared radiation and radiate energy at longer wavelengths (associated with the lower temperatures at the cirrus cloud heights) in all directions. The energy radiated downward by the cloud is put back into the system, warming the levels beneath the cloud, while a reduced amount of upwelling infrared radiation leaves the system. Since the effective temperature of the planet is dependent upon the balance between the incoming and outgoing radiation, the change in the radiation balance caused by cirrus clouds has to be understood to predict future climate change.

The cirrus cloud morphological and optical properties alter the Earths radiation balance. The cloud structural properties which affect the radiation balance are: the cloud height, latitude, and the frequency of cloud occurrence. The height of the cirrus cloud governs its radiative temperature. Since the cirrus cloud height, the insolation, and the Earths surface temperature are functions of latitude, the effect of cirrus clouds on the radiative balance also changes with latitude (Platt (1981), p. 674-676). The frequency of occurrence of the cirrus clouds will control the overall impact of these clouds on the radiative balance. The more often cirrus clouds occur, the greater their effect will be on the global energy balance. The optical properties of the cirrus clouds moderate both the incoming and the outgoing radiation. The scattering properties of ice crystals at visible wavelengths control the amount of downwelling solar radiation reaching the lower atmosphere while the absorptive and scattering properties of the ice crystals at infrared wavelengths governs the amount of infrared radiation escaping to space.

Climatologies have been compiled to determine the cirrus cloud frequency

around the planet. Although there have been many cloud climatologies over the years, few have dealt with cirrus cloud coverage. One of the first extensive cloud climatologies to include cirrus clouds was compiled by London (1957). He assembled a large number of surface cloud observations from the Northern Hemisphere recorded in the 1930's and the 1940's and separated them according to cloud types, one of which was cirrus clouds. Recent climatologies have been compiled by Barton (1983), Woodbury and McCormick (1986), Prabhakara et al. (1988), Wylie and Menzel (1989), and Warren (1985). While the instruments and techniques used in these studies differ, each of these climatologies is limited by a lack of detailed global coverage. One cirrus climatology which was not regionally limited was compiled by Wylie et al. (1993). This four year cloud climatology used the NOAA polar orbiting HIRS (High resolution Infrared Radiation Sounder) multispectral infrared data. The cirrus clouds, detected using the CO_2 slicing technique (Smith and Platt (1978), p. 1797–1798), were present in 42% of the satellite observations on the average.

Cirrus cloud climatologies have been compiled from ground based point measurements and area averaged satellite data. The satellite and ground based instruments measure different atmospheric scales. The satellite climatology compiled by Wylie et al. (1993) averages 20 km by 20 km pixels containing cirrus clouds to produce 2° latitude by 3° longitude grids. The ground based point measurements observed only a small portion of the atmospheric structure (which may or may not contain cirrus clouds) which is advected over the instrument position. The cirrus cloud structure on a scale between the point measurements and the area averaged satellite measurements, the mesoscale, is unknown. In some cases, the mesoscale cirrus cloud structure has been inferred from point measurements. To ascertain the variability of the cirrus clouds on this intermediate scale, and thereby the accuracy of cirrus cloud point measurements in determining the overall cirrus cloud structure, cirrus clouds have to be measured throughout a mesoscale volume. One instrument capable of making these measurements is a volume imaging lidar.

The cirrus cloud optical properties, which depend directly upon the particle

composition, shape, size, and number density, also affect the Earths radiation budget. In situ measurements have been used to determine the cirrus cloud particle composition, size, shape, and number density. Cirrus clouds consist of ice crystals with maximum lengths typically in the range of 20-2000 μm (Liou (1986), p. 1172). These crystals are large compared to visible wavelength radiation and are approximately equal to or greater than the wavelengths of infrared radiation.

A relationship has been used by climate modelers to parameterize the cirrus cloud visible and infrared optical properties. From Mie theory, as a spherical particle becomes large compared to the wavelength of the incident light, the scattering efficiency of the particle converges to two while the absorption efficiency of the particle converges to one (Liou (1980), p. 139). Since the cirrus cloud ice crystals are large compared to the wavelength of visible radiation and since the complex part of the index of refraction (which is associated with absorption by the particle) at visible wavelengths is small, scattering will dominate the interaction of solar radiation with the ice crystals. At infrared wavelengths, absorption will dominate the interaction between the ice particles and the radiation since the cirrus cloud ice crystals are highly absorbing at 10 μm (Dorsey (1940), p. 491). Due to the differing radiative properties of the ice crystals at the two wavelengths, the cirrus cloud optical properties at visible and infrared wavelengths has be related through Mie theory by a ratio of efficiencies, the scattering efficiency divided by the absorption efficiency. This ratio is approximately two when the particle absorption equals the particle emission at infrared wavelengths. This efficiency ratio can also be stated in terms of the cirrus cloud optical depth at the two different wavelengths: the visible scattering optical depth divided by the infrared absorption optical depth multiplied by a ratio of visible extinction efficiency to the infrared extinction efficiency. Both models and cirrus cloud measurements have been used to test this optical depth relationship for nonspherical ice crystals. A model Minnis (1991) used three size distributions of hexagonal ice crystals and calculated a ratio for the optical depths ranging from 2.06 to 2.22. For these calculations, it was assumed that the extinction efficiencies at the two wavelengths were equal.

Measurements from a FIRE (First ISCCP Cloud Climatology Project) IFO (Intensive Field Operation) which used ground based and satellite based instruments suggested a 2.13 ratio between the visible and infrared optical depths for the cirrus clouds (Minnis et al. (1990)). To calculate the visible optical depths for the FIRE data from the measured visible radiances, the ground albedo and the cloud cover within each pixel had to be known. Measurements by Platt et al. (1980) from a ground based lidar and satellite radiometers suggested a ratio less than 2.0. A method is described in this thesis which allows for the calculation of the visible optical depths for cirrus clouds in a mesoscale volume using a ground based volume imaging lidar. Knowledge of the cirrus cloud visible optical depths over a mesoscale region allows for a direct comparison with the cirrus cloud infrared optical depths measured by satellite radiometers for the same region. This method of comparing the cirrus clouds on the mesoscale can also be used to validate the cirrus cloud detection techniques from satellite radiometers.

This thesis quantitatively describes the variability of the cirrus cloud optical and morphological properties within a mesoscale volume measured by the University of Wisconsin Volume Imaging Lidar (VIL). The cirrus cloud cover within the measured volume is calculated and compared to cirrus cloud point measurements made with the University of Wisconsin High Spectral Resolution Lidar (HSRL). The difference between the point and area cloud covers is used to illustrate the importance of sampling errors in single point measurements when they are used to describe cirrus clouds throughout a mesoscale volume. This is accomplished by estimating the change in solar flux at the surface of the Earth using the difference in the average cloud cover detected by the two lidars and the measured cirrus cloud visible optical depths. The visible scattering properties of the cirrus clouds are also calculated throughout the mesoscale volume. This is achieved by directly calibrating the VIL backscattered signal to the cirrus cloud aerosol backscatter cross sections measured by the HSRL. This is possible since both instruments were aligned to simultaneously view the same cirrus clouds. The variability of the cirrus cloud aerosol backscatter cross sections will be determined using the

calibrated VIL signal within the mesoscale volume. The cirrus cloud visible scattering properties can then be used to calculate the visible optical depth of the cirrus clouds in the volume. These visible optical depths will then be directly compared to the infrared optical depths for the cirrus clouds calculated from VAS (VISSR Atmospheric Sounder) radiance measurements. The ratio of the visible and infrared optical depths is compared to Mie theory and results from previous experiments.

2 Instrumentation

The instruments used in this study are the University of Wisconsin High Spectral Resolution Lidar (HSRL), the University of Wisconsin Volume Imaging Lidar (VIL), and the VISSR (Visible and Infrared Spin Scan Radiometer) Atmospheric Sounder (VAS) situated on the GOES satellite. These instruments were part of CRSPE (University of Wisconsin–Madison Cirrus Remote Sensing Pilot Experiment) (Ackerman et al. (1993)).

2.1 HSRL

The HSRL is a dual channel vertically pointing lidar with high spectral resolution. This instrument makes point measurements (line measurements in time) of the atmospheric structure advected over its position by the wind. The HSRL transmits radiation at a wavelength of 532 nm and was used to determine the visible aerosol backscatter cross sections per unit volume, optical depths, and if the particulate and gaseous absorption are negligible, aerosol backscatter phase functions. The HSRL has an advantage over single channel lidar systems because it separates the backscattered radiation into a part due to aerosols and a part due to molecules. This separation is possible because the signal backscattered from the molecules is Doppler broadened while the larger, bulkier aerosols have little effect on the wavelength of the scattered light. This two channel approach enables

a direct calculation of the atmospheric extinction and aerosol backscatter cross sections per unit volume. The advantage of this system over a single channel lidar system can be seen by first examining the single channel lidar equation and then the dual channel lidar equation. The equation for a single channel lidar system is:

$$P(R) = \frac{E_o c A_r}{2R^2} [\beta_a'(180, R) + \beta_m'(180, R)] \exp^{-2 \int_0^R \beta_\epsilon(r') dr'} + M(R) + b \quad (1)$$

where:

R =   range (m)

$P(R)$ =   power incident on (and within the field of view of) the receiver within the spectral bandpass of the instrument (W)

E_o =   transmitted energy (J)

c =   speed of light (m s^{-1})

A_r =   area of the receiver (m^2)

$\beta_a'(180, R)$ =   aerosol backscatter cross section per unit volume (m^{-1} sr^{-1}) where:

$$\beta_a'(180, R) = \beta_a(R) \frac{P_a(180, R)}{4\pi} \quad (2)$$

$\beta_a(R)$ =   aerosol scattering cross section per unit volume (m^{-1})

$\frac{P_a(180, R)}{4\pi}$ =   aerosol backscatter phase function (sr^{-1})

$\beta_m'(180, R)$ =   molecular backscatter cross section per unit volume (m^{-1} sr^{-1}) where:

$$\beta_m'(180, R) = \beta_m(R) \frac{3}{8\pi} \quad (3)$$

$\beta_m(R)$ = molecular scattering cross section per unit volume (m^{-1})

$\frac{3}{8\pi}$ = molecular backscatter phase function (sr^{-1})

$\beta_\epsilon(R)$ = extinction cross section per unit volume (m^{-1})

$M(R)$ = multiple scattering contribution incident on the receiver within the field of view of the instrument (W)

b = background radiation incident on the receiver within the bandpass and field of view of the receiver (W)

Equation 1 contains two unknowns, $\beta_a'(180, R)$ and $\beta_\epsilon(R)$ (since $\beta_m(R)$ can be calculated from a radiosonde profile). This equation can be solved by either finding a relationship between $\beta_a'(180, R)$ and $\beta_\epsilon(R)$ or by using a calibration source to directly determine one of these two variables. In the former case, the Klett method has been used to solve the lidar equation. This method assumes a power law relationship between $\beta_a'(180, R)$ and $\beta_\epsilon(R)$ (Klett (1981)):

$$\beta_a'(180, R) = const \cdot \beta_\epsilon^k(R) \qquad (4)$$

where k, which is generally in the interval $0.67 \leq k \leq 1.0$ (Klett (1981), p. 212), depends on both the lidar wavelength and various aerosol properties which include the aerosol shape, composition, and number distribution. The power law relationship can be substituted into the differential form of the logarithmic lidar equation:

$$\frac{dS(R)}{dR} = \frac{1}{\beta_a'(180, R)} \frac{d\beta_a'(180, R)}{dR} - 2\beta_\epsilon(R) \qquad (5)$$

where:

$$S(R) = \ln\left(\frac{R^2 P(R)}{E_o}\right) \qquad (6)$$

to get the following nonlinear ordinary differential equation:

$$\frac{dS(R)}{dR} = \frac{k}{\beta_\epsilon(R)} \frac{d\beta_\epsilon(R)}{dR} - 2\beta_\epsilon(R). \tag{7}$$

This equation has the same form as the Bernoulli equation and is easily solved. If k is assumed to be a constant, then the solution to Equation 7 is:

$$\beta_\epsilon = \frac{\exp[(S - S_m)/k]}{\left\{\beta_{m\epsilon}^{-1} - \frac{2}{k} \int_r^{r_m} \exp[(S - S_m)/k]dr'\right\}} \tag{8}$$

where $S_m = S(r_m)$ and $\beta_{m\epsilon} = \beta_\epsilon(r_m)$ (Klett (1981), p. 213). This solution assumes that the backscatter by the atmospheric aerosols dominates the molecular backscatter. At 1064 nm, the wavelength of the VIL, this assumption is valid and Equation 8 can be used to solve the lidar equation. To maintain the stability and accuracy of the solution, Equation 8 has to be integrated backwards from far ranges. The dependence of this form of the solution on $\beta_{m\epsilon}$ decreases with decreasing r.

Equation 1 can also be solved by using a calibration source. Previous studies have used the lidar signal above or below cirrus clouds as the calibration source. It has been assumed that the backscattered radiation at the chosen height was the result of only molecular scattering (Sassen (1989)). This method used a constant multiple scattering correction factor and made an additional assumption for a constant backscatter to extinction ratio for the cirrus particles. Uncertainties in this method are largely due to aerosols in the calibration layer which cause a larger than expected signal for the molecular backscatter. This leads to smaller than expected aerosol backscatter cross sections which cause underestimates in the cirrus cloud visible optical depth calculations.

For the two channel approach used by the HSRL, Equation 1 was separated into two equations: one for molecular backscatter and one for aerosol backscatter (Shipley et al. (1983)):

$$N_m(R)R^2 = \frac{N_o c}{2} A_r \beta_m(R) \frac{3}{8\pi} \exp^{-2 \int_0^R \beta_\epsilon(r')dr'} \qquad (9)$$

$$N_a(R)R^2 = \frac{N_o c}{2} A_r \beta_a(R) \frac{P_a(180, R)}{4\pi} \exp^{-2 \int_0^R \beta_\epsilon(r')dr'} \qquad (10)$$

where:

$N_m(R)$ = number of incident photons on the receiver per unit time which were scattered by molecules from range R

$N_a(R)$ = number of incident photons on the receiver per unit time which were scattered by aerosols from range R

N_o = number of transmitted photons

$\beta'_m(180, R)$ = molecular backscattering cross section per unit volume (m^{-1} sr^{-1}) which depends upon the pressure and temperature of the air with height:

$$\beta'_m(180, R) = \frac{p(R)C_{air}}{T(R)} \qquad (11)$$

where:

$p(R)$ = air pressure at range R (Pa)

$T(R)$ = air temperature at range R (°K)

C_{air} = $4.51944 \cdot 10^{-9}$ °K Pa^{-1} m^{-1} sr^{-1} (at 532 nm).

A rawinsonde profile gives the needed information to solve Equation 11. Using the calculated $\beta_m(R)$ at each range (using Equation 3 and Equation 11), $\beta_\epsilon(R)$ can be determined by inverting Equation 9:

$$\beta_\epsilon(R) = -\frac{1}{2}\left[\frac{d(\ln(N_m(R)R^2)))}{dR} - \frac{d(\ln(\beta_m(R)))}{dR}\right]. \qquad (12)$$

Equation 11 gives a calibrated target at every range. This calibration target can be used to solve for the aerosol backscatter cross section per unit volume by

taking the ratio of the two scattering equations (Equation 9 and Equation 10) and rearranging terms:

$$\beta_a'(180, R) = \beta_m(R)\frac{3}{8\pi}\frac{N_a(R)}{N_m(R)}. \tag{13}$$

If gaseous and particulate absorption are negligible (extinction is just a result of scattering processes) then the aerosol scattering cross section is:

$$\beta_a(R) = \beta_\epsilon(R) - \beta_m(R). \tag{14}$$

The integration of $\beta_\epsilon(R)$ with range determines the aerosol visible optical depth (τ_v):

$$\tau_v = \int_0^R \beta_\epsilon(r')dr'. \tag{15}$$

Knowledge of $\beta_a(R)$ enables the calculation of the aerosol backscatter phase function:

$$\frac{P_a(180, R)}{4\pi} = \beta_m(R)\frac{3}{8\pi}\frac{N_a(R)}{\beta_a(R)N_m(R)}. \tag{16}$$

This set of equations shows the advantage of the HSRL over a single channel lidar system. The HSRL configuration allows for the direct calculation of the cirrus cloud visible optical depth, aerosol backscatter cross sections, and aerosol backscatter phase functions (if gaseous and particulate absorption are negligible).

2.2 VIL

The VIL is an elastic backscatter lidar which measures the three dimensional atmospheric structure. This instrument scans the atmosphere in both azimuth and elevation angles using a wavelength of 1064 nm. The VIL typically scans the

atmospheric structure in two directions, parallel and perpendicular to the wind direction at the cirrus cloud heights. A series of cross wind scans enables a three dimensional reconstruction of the cirrus clouds. This three dimensional view, using the advection of the clouds by the wind as the third dimension, reveals the cirrus mesoscale cloud morphology.

For CRSPE, the VIL scanned the atmosphere at approximately $9°$ a second with a time resolution of 85 seconds between consecutive scans. A typical VIL cirrus scan can be seen in Figure 1. The top cloud picture is a cross wind scan and the bottom picture is an along wind scan. The cross wind scan started at $357°$ (north), scanned overhead, and ended at $177°$. This is called the cross wind scan because it was almost perpendicular to the wind direction at the cirrus cloud heights (the wind was approximately from the west-northwest at the cirrus cloud heights). After the completion of the cross wind scan, the azimuth angle of the system was rotated $90°$ to begin the along wind scan. This scan started at $267°$, scanned overhead, and completed at $87°$ (toward the east). This X scan was performed almost continuously for a three hour time period (18:08 - 21:20 GMT). For CRSPE, the VIL scanned 120 km of the atmosphere in the horizontal extent with a maximum distance between data points of 60 m.

The two VIL scan directions allow for two different views of the cirrus clouds. Precipitation from the cirrus clouds can be seen in the along wind scan due to the wind shear at the cirrus cloud heights. This can be seen in the bottom picture in Figure 1. The slope of the cirrus clouds with distance results from wind shear. The along wind scan also shows the cirrus clouds which will be advected over the VIL at later times. The cross wind scans show the cirrus cloud structure perpendicular to the wind. The cirrus clouds seen in the cross wind scans during this experiment usually had a higher degree of spatial variability than those observed in the along wind scans. These variations across the wind would not be seen by a vertically pointing ground based instrument.
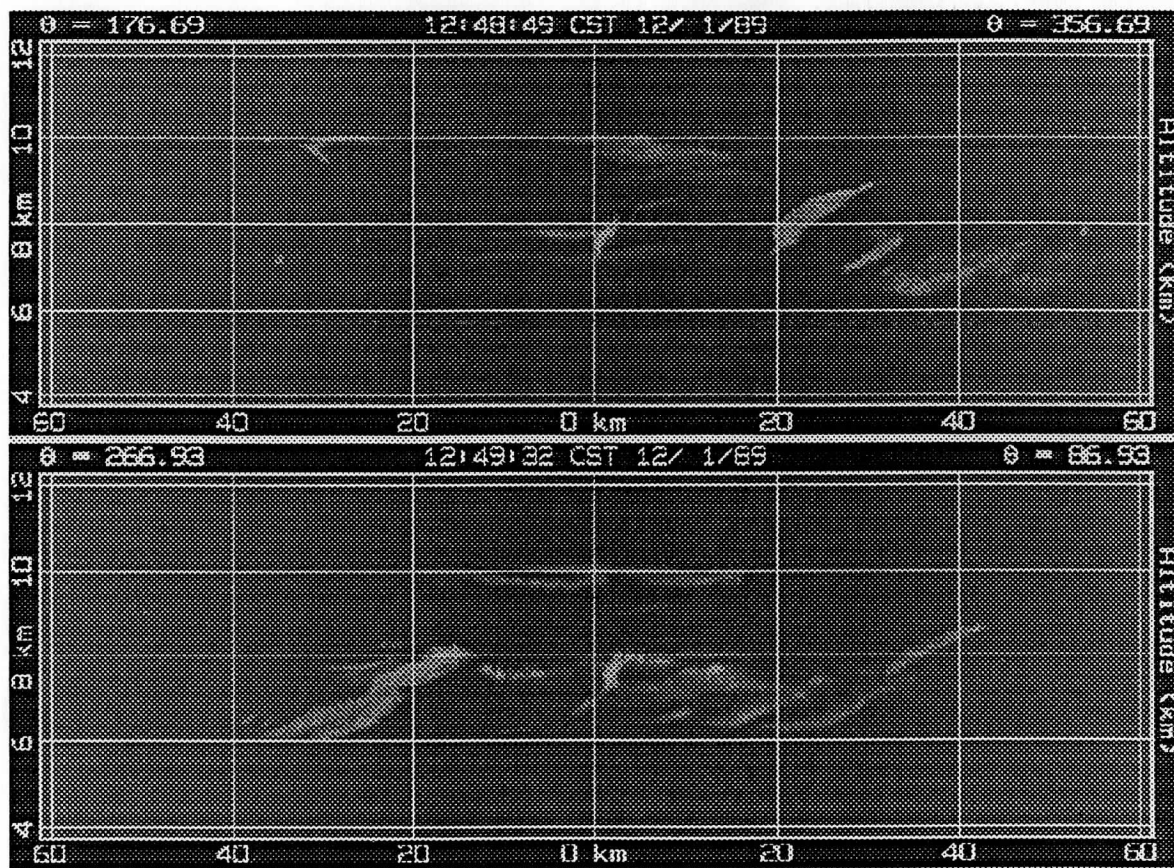
Figure 1: Typical cirrus clouds seen from 18:08 to 19:24 GMT. The x-axis is the distance from the VIL and the y-axis is height. The top picture is a cross wind scan; scanning from the North (357°) to the South (177°). The bottom picture is an along wind scan, scanning from West (267°) to East (87°). The scan times are given in local time (CST). Both scans show the cirrus cloud variability. Precipitating cirrus clouds are seen in the along wind scan.

2.3 VAS

The VAS, a radiometer on the GOES satellite, detects infrared radiation in 12 spectral bands that lie between 3.9 and 15 μm at 7 km or 14 km resolution (depending on the detector used) while also measuring at visible wavelengths with a 1 km resolution. The infrared channels have a 7 km resolution at nadir above the equator and a 10 km resolution viewing the atmosphere above Madison, Wisconsin. The upwelling longwave radiation in the 11 μm channel was used to determine the cirrus cloud infrared emissivity and optical depth. The upwelling radiation was converted into a temperature for each pixel using Planck's Radiation Law. The cirrus infrared emissivity was then calculated using the following equation:

$$\epsilon_{ir} = \frac{T_{sfc}^4 - T_{sat}^4}{T_{sfc}^4 - T_{cld}^4} \tag{17}$$

where:

T_{sfc} = brightness temperature for a clear pixel
T_{sat} = brightness temperature detected by the radiometer
T_{cld} = temperature at the mid-cloud height.

T_{sfc} used in Equation 17 was determined from a satellite pixel where it was assumed that no clouds were present (a clear pixel). Clear pixels were determined with help from the VIL since subvisible cirrus clouds were present during the experiment. The cirrus mid-cloud heights were calculated from the VIL cross wind scans. The cloud temperatures associated with the cirrus mid-cloud height were determined from coincident rawinsonde measurements. The rawinsondes were launched from the HSRL site during this experiment.

2.4 Instrumentation Locations

For CRSPE, the VIL was located near Pine Bluff, Wisconsin (43.06° N Latitude and 270.30° E Longitude) while the HSRL was located to the east in Madison,

Wisconsin (43.08° N Latitude and 270.58° E Longitude). The HSRL was located a distance of 24 km from the VIL at an azimuth of 87° (1.26 km North and 23.97 km East of the VIL). One of the VIL scan planes was aligned over the position of the HSRL viewing the same cirrus clouds as the HSRL. In relation to Pine Bluff, Wisconsin, the VAS was situated at a zenith angle of 52.90°, an azimuth angle of 244.58°, and a distance of 38017.73 km. The time periods of the experiment under investigation are from 18:07 to 19:24 GMT and from 19:29 to 21:20 GMT on December 1, 1989. The separation of the time periods was a result of a break in the VIL data set. The wind speed, wind direction, temperature, and pressure at the cirrus cloud heights were determined from coinciding rawinsonde profiles. There were four rawinsondes launched from Madison, Wisconsin on December 1, 1989, two of which were used: 18:00 GMT and 21:24 GMT. To create individual profiles between these times, the rawinsonde data was linearly interpolated between the 18:00 and 21:24 profiles.

Three remote sensing instruments were used to determine the cirrus cloud optical and structural properties. The VIL was used to determine the cirrus cloud structural properties since it viewed the three dimensional cirrus cloud structure. Cirrus cloud cover percentages and horizontal structure functions were calculated from the three dimensional data. The VIL area averaged cirrus cloud structure was compared to the cirrus cloud structure measured by the HSRL. This allowed for the determination of the sampling errors associated with cirrus cloud point measurements. To calculate the cirrus cloud optical properties, all three remote sensing instruments were used. The HSRL was used to calibrate the VIL to determine the visible cirrus cloud optical properties throughout a mesoscale volume. The VAS was used to determine the infrared cirrus cloud optical properties for the same volume.

3   Cirrus Cloud Mesoscale Structure

Many previous measurements of the cirrus cloud morphology have been made using ground based vertically pointing instruments. These cloud measurements were aligned along the wind due to the advection of atmospheric structure over the instrument. Attempts by these point measurements to represent the general cirrus cloud structure relied on the uniformity of the clouds throughout the area under consideration. If the cirrus clouds varied significantly across the wind, then point measurements along the wind could not be used to represent the large scale cirrus cloud structure. The VIL cirrus cloud scans were used to observe the cirrus cloud structure in an atmospheric mesoscale volume. Cirrus cloud structural variations within this volume were used to determine the cirrus cloud variability and the sampling errors associated with cirrus cloud point measurements.

During CRSPE, the VIL scanned a volume of the atmosphere containing cirrus clouds. Each cross wind scan showed a two dimensional picture of the cirrus clouds. A time series of cross wind scans revealed the three dimensional cloud structure where it was assumed that there was no time variation during the advection of the cirrus clouds by the wind. Once a cirrus cloud threshold value was chosen for the VIL data within the volume, the cloud cover percentage and horizontal structure within the mesoscale volume could be calculated from consecutive cross wind scans. A cirrus cloud threshold denotes the smallest backscattered signal considered to be from a cirrus cloud. A threshold value was determined by examining a histogram of the VIL backscattered signal from the cirrus cloud heights, 6 to 11 km, for the time periods under consideration (Figure 2). A clear distinction between cirrus cloud backscatter and the background aerosol backscatter was seen. The range squared, energy normalized VIL data greater than the chosen threshold value (3.48 in Figure 2) was assumed to have been backscattered from the cirrus cloud ice crystals. Backscatter values smaller than the threshold were considered to be the result of non-cirrus aerosols and molecules. Since the threshold was chosen from a series of VIL cross wind scans, the cirrus cloud

threshold value was constant for the whole data set. Only data within a horizontal distance of 30 km from the VIL was used in the cirrus cloud determination. The 30 km distance was chosen to retain a consistent threshold value throughout the data set. When the distance to the scatterers becomes large, the VIL signal becomes instrument limited causing the thinner cirrus clouds to go undetected. The calculations of the cirrus cloud structure are done in the following subsections.

3.1   Horizontal Cirrus Cloud Structure

The cirrus cloud threshold determined in the previous section allows the cirrus cloud structure to be examined. To calculate the cirrus cloud cover percentage within the mesoscale volume, RTI (Range Time Indicator) profiles were created at 100 m intervals along the VIL cross wind scan up to a distance of 30 km from the VIL. A RTI is a plot of the backscattered signal where time is the x-axis and altitude is the y-axis. A total of 601 RTIs were created for each time period. Consecutive points in each RTI were separated by 85.5 seconds, the time between consecutive cross wind scans. The cross wind scan time separation was converted into a distance by using the average wind speed measured by the rawinsonde at the cirrus cloud heights. An average wind speed of 35 ms^{-1} resulted in a distance between scans of approximately 3 km. The RTIs simulated 601 vertically pointing lidar systems situated across the wind at 100 m intervals. The cloud cover percentage from each RTI shows the cloud cover that would be observed by a vertically pointing lidar system at that position. To determine the presence of cirrus clouds, the VIL backscattered signal between the heights of 6 and 11 km in each simulated vertical profile was compared to the cirrus cloud threshold value. If any of the data points between the given heights for each vertical profile (for each simulated RTI) had a value greater than the cirrus cloud threshold value, then that RTI point contained cirrus clouds. Otherwise the point was labeled clear.

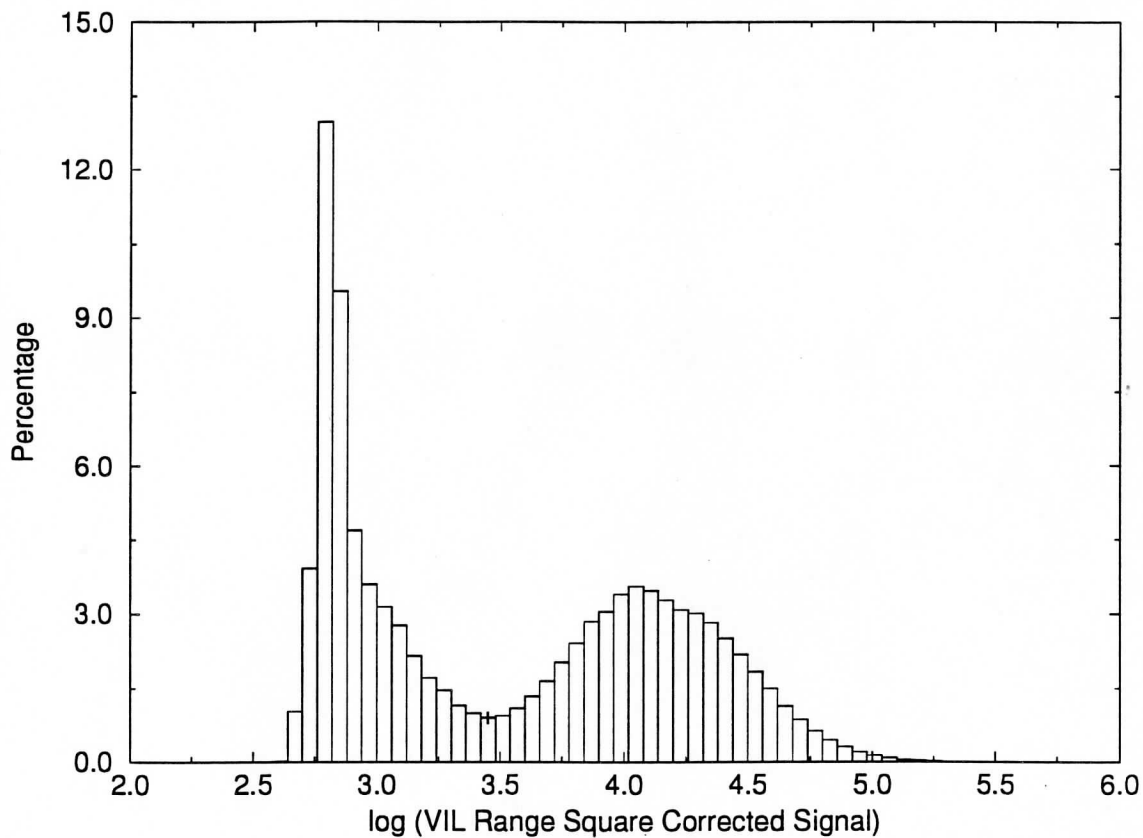Figure 2: 50 point histogram of the VIL signal from the cirrus cloud heights, 6 km to 11 km. The x-axis is the logarithm of the VIL range square corrected, energy normalized signal. The y-axis is the percentage of points in each interval. Notice the local minimum near 3.5. This shows a clear separation between the cirrus cloud ice crystal backscatter and the background aerosol and molecular backscatter at 1064 nm.

The cloud cover percentage calculated from the simulated RTIs was used to determine the spatial variability of cirrus clouds within a mesoscale volume. A direct comparison of average cloud cover seen by the VIL and the cloud cover detected by individual VIL RTIs shows the difference between point and area measurements of the cirrus cloud structure. Cirrus cloud-nocloud structure functions was calculated to determine the horizontal dimensions of the cirrus clouds and the distance separating the individual cloud structures. A cross wind structure function was used to determine the separation between and length of the cirrus clouds across the wind. An along wind structure function was used to determine the length of the cirrus clouds and the distances separating these clouds along the wind.

A three hour time period on December 1, 1989 was investigated. As described earlier, this three hour data set was split into two sections which were chosen as a result of the continuity of the VIL data. The first time period extended from 18:08 to 19:24 GMT and the second from 19:29 to 20:21 GMT on December 1, 1989. The earlier period contained a large amount of scattered cirrus clouds while the later period had some scattered cirrus clouds early but at 20:30 GMT a widespread precipitating cirrus cloud deck was advected into the region.

3.1.1 Cirrus Cloud Cover Percentage

Cirrus cloud cover percentages were calculated for the VIL simulated RTIs and the HSRL RTI for the two time periods. To compare the VIL and HSRL cloud cover percentage values, the HSRL data had to be shifted upwind to the position where the same cirrus clouds occurred in the VIL scans. This time shift ($\sim$10 minutes) was used to match the two data sets. The shift was determined from the distance between the two systems and the average wind speed at the cirrus cloud heights. The average wind direction at the cirrus cloud heights, determined by the rawinsonde, was used to calculate the direction to shift the HSRL data upwind. The HSRL shifted RTI and VIL simulated RTI cirrus cloud cover percentages were then compared for the two data periods.

For the first time period (18:08-19:24 GMT), broken cirrus clouds were advected into the region from 278° to 297° at wind speeds ranging from 26 ms^{-1} to 40 ms^{-1}. Cirrus cloud cover percentages were calculated for the 60 km of VIL vertical profiles spaced every 100 m (Figure 3). The individual RTIs show cirrus cloud cover percentages ranging from 54.7% 17.2 km south of the VIL to 100% both directly above the VIL and 30 km to the north of the VIL. The mean cloud cover was 81.5% for the mesoscale volume. The maximum difference in cloud cover between two RTIs in the 60 km spread was 45.3%. The maximum cloud cover difference between two RTIs 10 km apart was 27.8%. For the same time period, the time shifted HSRL data had a cloud cover percentage of 100%. Since the VIL along wind scan was not perpendicular to the wind axis, the cirrus clouds seen by the HSRL passed 5.54 km to the north of the VIL.

There are a couple of interesting features to note in Figure 3. A cloud cover percentage of 100% was seen directly above the VIL. This maximum was the result of a very thin cirrus cloud layer located at a height of 10 km, the tropopause. This high cloud cover percentage was the result of specular reflection from ice crystals. Specular reflection occurs when higher than normal signal is backscattered to the receiver due to specific ice crystal orientations. When the cirrus cloud ice crystals are in the form of plates they can become positioned such that their flat surfaces are parallel to the ground. This plate orientation causes enhanced laser backscatter when the lidar at the ground is viewing vertically. Directly above the VIL specular reflection occurred but the backscattered signal off the vertical did not show this enhanced backscatter. This reveals the importance of tilting the receiver of a vertically pointing lidar system slightly off of the vertical. For this early time period, the HSRL saw 100% cirrus cloud cover due to the oriented ice crystals. The VIL also detected signal from this height but the backscatter signal was smaller than the threshold value, causing the VIL to miss these clouds (except for the cases where specular reflection occurred). During this experiment, the HSRL was tilted off of the vertical to remove the occurance of specular reflection. The 100% cirrus cloud cover percentage seen by the HSRL shows that specular

reflection was a problem and that the HSRL receiver was not tilted as far off of the vertical as was originally thought.

A second interesting feature in Figure 3 was the variation of the cirrus clouds within the volume. By comparing the cirrus cloud cover at 17.2 km and 24.7 km to the south of the VIL, a cloud cover difference of 27.8% was seen. This difference shows the variability of cirrus clouds across a short distance (7.5 km) even when the cloud cover is averaged in time. This cirrus cloud variability shows possible sampling errors when point measurements are used to represent the cirrus cloud cover over an area. A point measurement made at either 17.2 km or 24.7 km south of the VIL could not accurately describe the general cirrus clouds structure within a mesoscale volume. This reveals the difficulties encountered when using a single vertically pointing system to describe the cirrus cloud spatial structure over a large area. The variation of cirrus clouds within a small region suggests a need to view cirrus clouds throughout the mesoscale volume.

Since cirrus clouds affect the incoming solar radiation, an error in the cirrus cloud cover percentage will result in changes in the calculated visible radiative flux reaching the surface of the Earth. The magnitude of the change in the calculated visible radiative flux will determine whether the cirrus cloud cover needs to be considered when discussing climate warming. To estimate the magnitude of this change in the incoming solar flux, consider a simple calculation for the change in the direct solar flux due to an incorrect cirrus cloud cover percentage:

$$\Delta F = \mu_o \frac{r_o^2}{r^2} \mid S_{con} \Delta P_{clr} + S_{con} \Delta P_{cld} T \mid \tag{18}$$
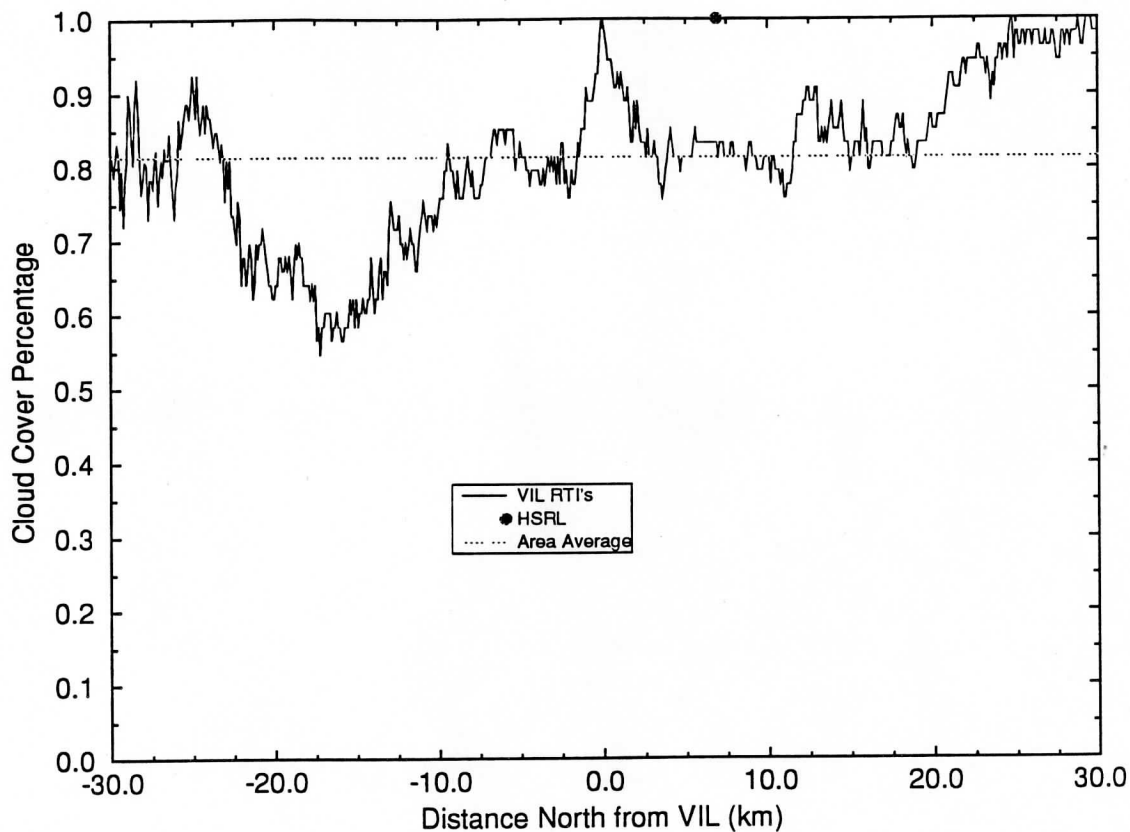
where:

Figure 3: Cloud cover percentages calculated for 601 simulated RTIs for the time period 18:08 to 19:24 GMT on December 1, 1989. The x-axis is the distance from the VIL (north is positive). The y-axis is the cloud cover percentage. The solid line is cloud cover percentages for each VIL simulated RTI (consecutive RTIs are separated by 100 meters). These cloud cover percentages are aligned along the wind resulting in a time average of the cirrus clouds for each RTI. The solid circle is the time shifted HSRL cloud cover percentage. The dashed line is the average VIL cloud cover percentage for this time period. Note the specular reflection directly above the VIL.

$$
\begin{aligned}
S_{con} &= \text{mean annual solar constant } (1380 \text{ W m}^{-2}) \\
\Delta P_{clr} &= \text{change in percentage of sky which is clear } (-\Delta P_{cld}) \\
\Delta P_{cld} &= \text{change in percentage of sky which is cloudy} \\
T &= \text{transmission through the cloud } (\exp(-\tau_{vis})) \\
\tau_{vis} &= \text{visible scattering optical depth} \\
\mu_o &= \text{cosine of the solar zenith angle} \\
r_o &= \text{mean Earth-Sun distance} \\
r &= \text{actual Earth-Sun distance}
\end{aligned}
$$

On the right hand side of Equation 18, the first term is the change in radiance produced from the transmission of the solar radiation through the cloudless atmosphere while the second term is the change in radiance error produced from the transmission of solar radiation through the cirrus clouds. The absolute value was taken because we are only interested in an estimate of the magnitude of the change of the incoming solar radiation, not whether warming or cooling would occur. For the Earth, μ_o is described as the following:

$$
\mu_o = \sin \delta \sin \phi + \cos \delta \cos \phi \cos \omega \tag{19}
$$

where ϕ is the latitude and δ is the solar declination angle which is defined as:

$$
\delta = 23.45 \sin \left(\frac{360^o}{365} (d_n + 284) \right) \tag{20}
$$

with d_n as the day of the year. The hour angle, ω, is defined as:

$$
\omega = -15^\circ H \tag{21}
$$

where H is number the of hours from local noon. $\frac{r_o^2}{r^2}$ can be rewritten in the following form:

$$\frac{r_o^2}{r^2} = 1 + 0.033 \cos\left(\frac{360^o d_n}{365}\right) \tag{22}$$

Equations 18 to 22 were used to estimate a change in the direct visible radiative flux seen at the surface of the earth due to an incorrect cirrus cloud cover. The cloud cover percentage error used for the first time period was the difference between the minimum and maximum VIL RTI cloud cover percentages. The HSRL cloud cover percentage for the same cirrus cloud deck was not used because of possible contamination by specular reflection. The absorption of solar radiation by the atmospheric constituents was neglected in these calculations. For the first time period, the transmissivity of the cirrus clouds at solar wavelengths was defined by the cirrus cloud visible optical depth measured by the HSRL, $\tau_{vis} = 0.257$.

An estimate of the change in solar flux at the surface of the earth for Madison, Wisconsin at 13:00 GMT on December 1, 1989 was calculated using Equation 18. For this time period, a 45.3% difference in cirrus cloud cover resulted in a change of 58.18 Wm^{-2} seen at the surface of the Earth. The magnitude of this error was approximately 14 times greater than the effects due to the doubling of CO_2, 4 Wm^{-2}. Obviously an incorrect cloud cover will have an important effect on both the radiative balances occurring in the atmosphere and the models simulating the radiative and dynamical structure of the Earth's atmosphere. Even though Equation 18 does not incorporate the Earth's surface albedo or absorption by atmospheric gases, it does show the need for the accurate simulation of cirrus clouds and their global coverage.

For the later time period (19:29 to 21:20 GMT), scattered cirrus clouds were present until 20:30 when a widespread, three kilometer thick, cirrus cloud deck was advected into the region from approximately 277°. The area averaged cloud cover for the VIL was 76.3%, 4.7% smaller than the previous time period. The HSRL cloud cover was 67.9% (Figure 4), resulting in a cloud cover difference between the two systems of 8.9%. The minimum cloud cover detected by a VIL RTI was 59.0%, from 0.7 to 1.0 km north of the system. The maximum detected cloud cover was 100%, 29.8 km to the north. A maximum cloud cover difference of

41.0% was seen between the VIL RTIs. The maximum cirrus cloud cover difference detected between RTIs separated by 10 km was 30.8%. Again large variations in the cloud cover were noticed depending on the location of a vertically pointing lidar. Specular reflection does not have as large of an effect on the cloud cover percentages because most of the cirrus clouds were lower and optically thicker than the previous time period. Also, the thin cirrus layer at the tropopause was not detected after 20:00 GMT.

By using Equation 18 for Madison, Wisconsin at 14:30 GMT on December 1, 1989, with an average $\tau_{vis} = 0.428$ for the cirrus clouds (measured by the HSRL), a change of 12.36 Wm^{-2} was seen at the surface of the Earth. This value was approximately five times smaller than the previous time period. The early time period had a large cloud cover difference and small optical depth. The latter had a smaller cloud cover difference and a larger optical depth. It also had less incident solar radiation due to the time of day. There were compensating effects during the second time period due to the larger optical depth and the smaller cloud cover difference. The larger cirrus cloud optical depth reduced the incoming solar radiation more than the earlier time period but the smaller cirrus cloud cover percentage difference decreased the effect of the cirrus clouds on the radiation balance. The change in the radiative flux caused by cirrus clouds for either time period would dominate the atmospheric temperature increases caused by the doubling of CO_2. This implies that knowledge of the spatial structure is very important in understanding the radiative effects of cirrus clouds on the climate.

As was previously shown, cirrus clouds can vary significantly over a mesoscale area. Very precise point measurements of cirrus clouds will not give reliable statistics of the cirrus clouds due to the cloud sampling errors. Better instruments which only measure a vertical profile through the atmosphere would not be able to accurately describe the influence of the cirrus cloud spatial structure on the climate because of the sampling errors. Even a very long time average would not give an accurate description of the cirrus clouds. The long time average would be biased

because the clouds have to be advected over the instrument. The cross wind cirrus cloud variation would not be detected, and, as shown previously, this can be significant (especially if the cirrus clouds tend to align along the wind direction). Although the VIL has been used to determine the cirrus cloud spatial structure throughout a mesoscale volume, the effects of this cirrus cloud variation on the Earth's radiation balance has yet to be determined.

In some models which simulate the effects of cirrus clouds on the Earth's radiation balance, the three dimensional cirrus clouds have been averaged to produce a cirrus cloud layer with the equivalent radiative properties, an 'equivalent uniform layer'. This reduction in complexity of the cirrus cloud radiative properties can be achieved for the radiative effects of the cirrus clouds at one wavelength of radiation according to the mean value theorem. Complexities arise in this process when the radiative effects of the cirrus clouds has to be described at two different wavelengths, say at both visible and infrared wavelengths. In this case, the radiative effects at both wavelengths have to be matched within the equivalent uniform layer of cirrus clouds, which may not be possible. Even if an equivalent uniform layer was used, the radiative properties of the cirrus clouds may be reproduced but the dynamical structure of the atmosphere would not be reproduced. Since clouds are an integral part of the atmosphere they affect both the radiative balance and the dynamical structure. An equivalent uniform cloud field will not have the same dynamical effect as multi-layered scattered cirrus cloud field. As an example, if a previously uniform cirrus cloud field was evaporating and breaking up, then there would be regions of subsidence within the cloud field. This will not be simulated in a model using an equivalent uniform layer as a parameterization for cirrus clouds.
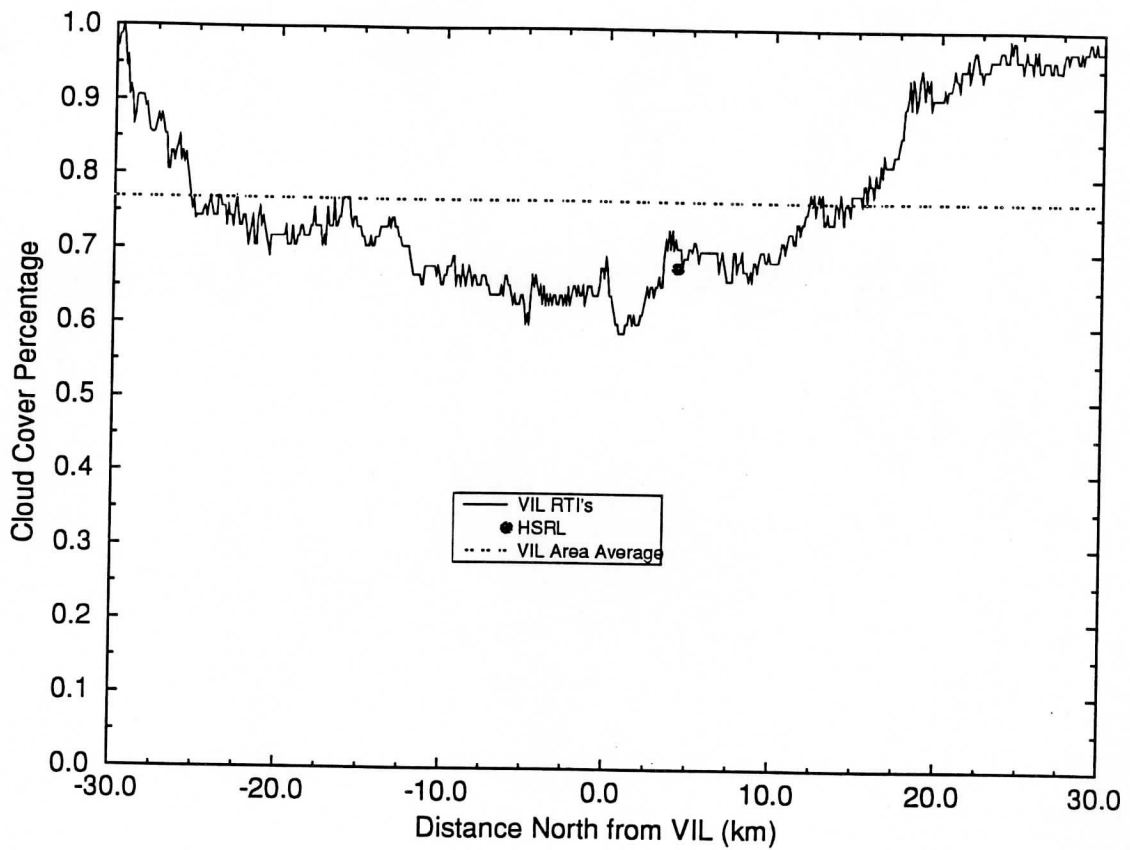
Figure 4: Same as Figure 3 except for the time period from 19:29 to 21:20 GMT on December 1, 1989.

3.1.2   Structure Functions

A cirrus cloud-nocloud horizontal structure function was calculated for the three hour time period, 18:08 - 21:20 GMT (Figure 5), using the following equation:

$$SF_{AA}(l) = \frac{1}{N-l} \sum_{k=0}^{N-l-1} [A_k - A_{k+l}]^2 \tag{23}$$

where:

A_k	=	the cloud-nocloud value (either 1 or 0) at point k
A_{k+l}	=	the cloud-nocloud value (either 1 or 0) value at the point $k+l$
l	=	lag
N	=	number of points

A maximum in the structure function shows a negative correlation between points separated by the lag, i.e. length of the cloud; a relative minimum indicates a positive correlation between points separated by the lag, i.e. the distance between clouds (except at zero separation which is defined to be zero). For the structure function, the width (or length) of the cloud occurs at a local maximum. This was not the half-width of the cloud because if the lag was equal to half the cloud length, an increase in the lag would cause an increase in the structure function. Structure functions were determined both along and across the wind. For the structure functions aligned with the wind, the lag was a function of time. This lag was converted into a distance using the average rawinsonde measured wind speed at the cirrus cloud heights. The along wind structure function was used to determine the length of the cirrus clouds and distance between cirrus clouds. For the cross wind structure functions, the lag was a function of distance. The cross wind structure functions shows the the length of the cirrus clouds and the distance between clouds across the wind.

A series of along wind structure functions were calculated for the 60 km of VIL data for the combined 3 hour time period (Figure 5). The plotted structure functions consist of individual structure functions 25 km north and south of the VIL, a structure function for the cirrus clouds occurring directly above the VIL, and an area averaged structure function. A large amount of variation between the individual structure functions was seen in Figure 5. The along wind structure function 25 km to the north revealed approximately a 6 km (3 minute) length for the cirrus clouds. This structure function had very little variation because 25 km to the north of the VIL the sky had over 95% cloud cover as seen in Figures 3 and 4. The structure function 25 km to the south of the VIL showed a separation between clouds of approximately 262 km (125 minutes) with a cirrus cloud length of 147 km (70 minutes). The cirrus clouds directly overhead had a separation of 262 km (125 minutes) with a 141 km (67 minutes) cloud length. The average structure function for the mesoscale region imaged by the VIL revealed a 273 km (130 minutes) separation between clouds and an average cloud length of 130 km (62 minutes). Smaller scale oscillations were embedded on the individual structure functions. These oscillations show small scale variations in the cirrus features. The effects of the area averaging can be seen in the average structure function where the small scale oscillations have been smoothed out. The half width of the cirrus cloud, 65 km, shows the average distance that a satellite has to move its field of view along the wind direction to view the ground. If a vertically pointing system were used to determine the cirrus cloud structure, the result would be a single structure function defining the whole region. As was seen here, this would not be representative of the volume.

The average cross wind structure function is shown in Figure 6. This structure function increases slowly with the lag because a greater percentage of the cirrus clouds occurred to the north of the VIL. The movement of a widespread cirrus cloud deck from the northwest into a region which previously contained scattered cirrus clouds biased the structure function to larger lag distances. The average

3.1.2 Structure Functions

A cirrus cloud-nocloud horizontal structure function was calculated for the three hour time period, 18:08 - 21:20 GMT (Figure 5), using the following equation:

$$SF_{AA}(l) = \frac{1}{N-l} \sum_{k=0}^{N-l-1} [A_k - A_{k+l}]^2 \tag{23}$$

where:

A_k	=	the cloud-nocloud value (either 1 or 0) at point k
A_{k+l}	=	the cloud-nocloud value (either 1 or 0) value at the point $k + l$
l	=	lag
N	=	number of points

A maximum in the structure function shows a negative correlation between points separated by the lag, i.e. length of the cloud; a relative minimum indicates a positive correlation between points separated by the lag, i.e. the distance between clouds (except at zero separation which is defined to be zero). For the structure function, the width (or length) of the cloud occurs at a local maximum. This was not the half-width of the cloud because if the lag was equal to half the cloud length, an increase in the lag would cause an increase in the structure function. Structure functions were determined both along and across the wind. For the structure functions aligned with the wind, the lag was a function of time. This lag was converted into a distance using the average rawinsonde measured wind speed at the cirrus cloud heights. The along wind structure function was used to determine the length of the cirrus clouds and distance between cirrus clouds. For the cross wind structure functions, the lag was a function of distance. The cross wind structure functions shows the the length of the cirrus clouds and the distance between clouds across the wind.

A series of along wind structure functions were calculated for the 60 km of VIL data for the combined 3 hour time period (Figure 5). The plotted structure functions consist of individual structure functions 25 km north and south of the VIL, a structure function for the cirrus clouds occurring directly above the VIL, and an area averaged structure function. A large amount of variation between the individual structure functions was seen in Figure 5. The along wind structure function 25 km to the north revealed approximately a 6 km (3 minute) length for the cirrus clouds. This structure function had very little variation because 25 km to the north of the VIL the sky had over 95% cloud cover as seen in Figures 3 and 4. The structure function 25 km to the south of the VIL showed a separation between clouds of approximately 262 km (125 minutes) with a cirrus cloud length of 147 km (70 minutes). The cirrus clouds directly overhead had a separation of 262 km (125 minutes) with a 141 km (67 minutes) cloud length. The average structure function for the mesoscale region imaged by the VIL revealed a 273 km (130 minutes) separation between clouds and an average cloud length of 130 km (62 minutes). Smaller scale oscillations were embedded on the individual structure functions. These oscillations show small scale variations in the cirrus features. The effects of the area averaging can be seen in the average structure function where the small scale oscillations have been smoothed out. The half width of the cirrus cloud, 65 km, shows the average distance that a satellite has to move its field of view along the wind direction to view the ground. If a vertically pointing system were used to determine the cirrus cloud structure, the result would be a single structure function defining the whole region. As was seen here, this would not be representative of the volume.

The average cross wind structure function is shown in Figure 6. This structure function increases slowly with the lag because a greater percentage of the cirrus clouds occurred to the north of the VIL. The movement of a widespread cirrus cloud deck from the northwest into a region which previously contained scattered cirrus clouds biased the structure function to larger lag distances. The average
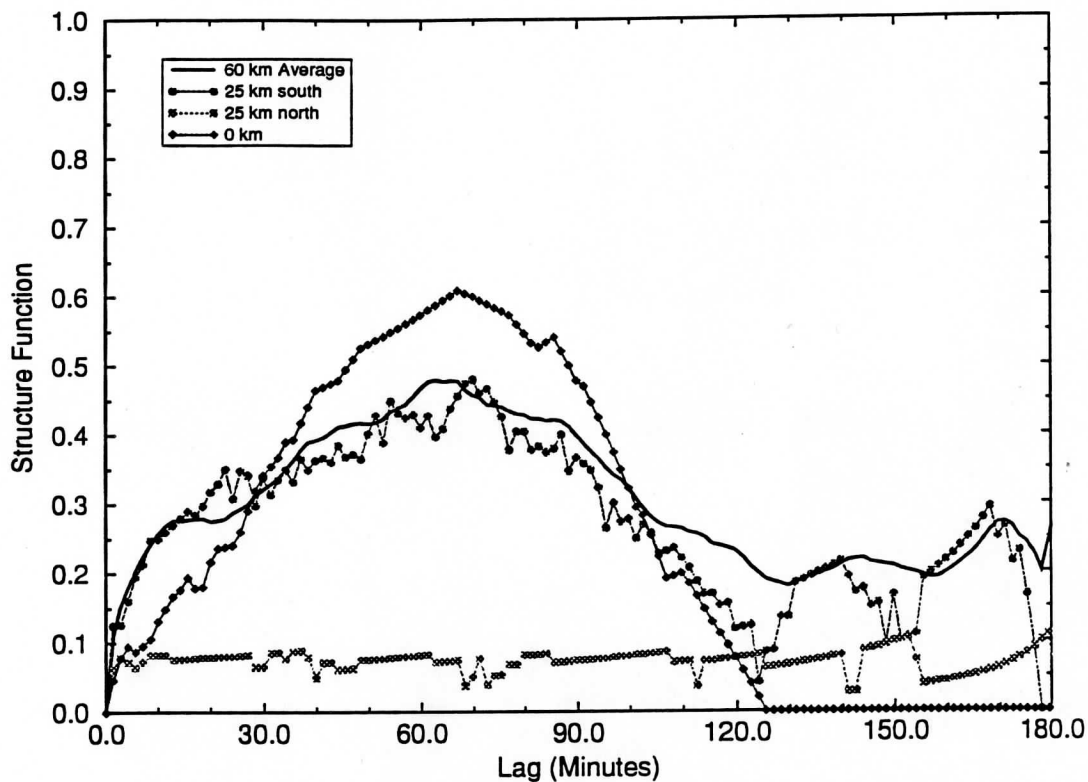
Figure 5: Along wind structure functions for December 1, 1989, from 18:08 to 21:20 GMT, calculated from the VIL simulated RTIs. The x-axis is the lag in the structure function in minutes (1 minute is approximately 2100 meters). The y-axis is the cloud-nocloud structure function. Plotted are: the average along wind structure function for the 60 km spread (thick solid line), structure function for a RTI 25 km south of the VIL (circles), structure function for an RTI 25 km north of the VIL (squares), VIL structure function for a RTI directly overhead (diamonds). More detailed explanations are in the text.

cross wind structure function shows cirrus clouds with lengths of 14 km and 43 km. The distance between cirrus clouds was 24 km. As expected, the cross wind structure function was very different than the along wind structure function during this time period. The length of the cirrus clouds along the wind was about 9 times larger than the cirrus cloud length across the wind. The difference in the average structure functions for the two scan directions results in an aspect ratio (length/width) of 9:1 for the cirrus clouds. This aspect ratio suggests that, for this experiment, the cirrus clouds tended to be aligned along the wind. A longer time period has to be analyzed to get a better understanding of the average cirrus cloud horizontal structure.

To get a statistically accurate measurement of the distance between clouds the structure function has to become either independent of the lag or a constant which is periodic with the lag. This was only seen for the individual cirrus cloud structure function 25 km to the north of the VIL. The other structure functions gave local measurements of the cirrus cloud structure since the structure function varied with the lag. A longer time period is needed to get better cloud cover statistics for the structure function calculations. This process can be performed on the FIRE II VIL data set.

3.2 Vertical Cirrus Cloud Structure

The vertical cirrus cloud structure during the two time periods was very complex. From 18:08-19:24 GMT, there was mostly scattered optically thin cirrus clouds which occurred both individually and in layers as seen in Figure 1. The lowest level clouds occurred at a height of 6 km while the highest cirrus clouds were seen at 10 km. The uppermost clouds occurred at the tropopause and consisted of ice crystals as seen by the specular reflection from the layer (as described in Section 3.1.1). The majority of the cirrus clouds occurred between the heights of 6 and 9 km, often overlapping at different levels. Occasionally, a precipitating
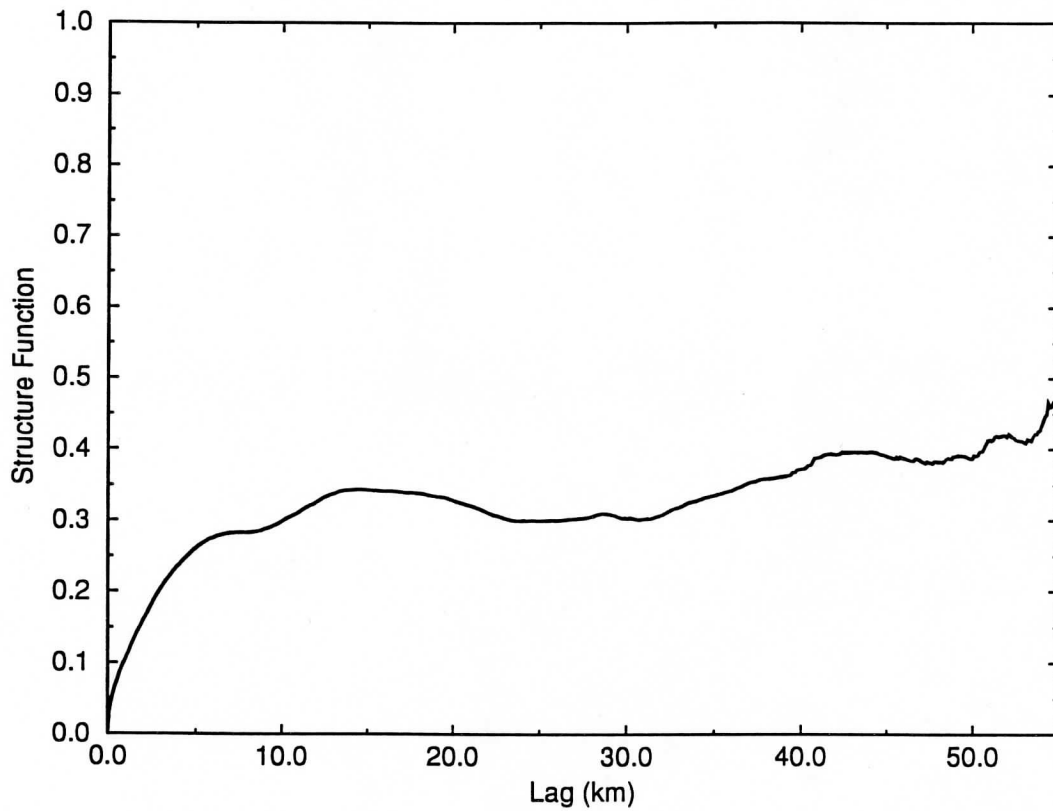
Figure 6: Cross wind structure function for December 1, 1989, from 18:08 to 21:20 GMT, for the 60 km of VIL data. The x-axis is the lag in the structure function in distance (km). The y-axis is the cloud-nocloud structure function. This plot shows the average cross wind structure function for the 3 hour time period. The minimum around 24 km shows the average distance between the cirrus clouds. The peak determines an average cirrus cloud cross wind length of 14 km.

cirrus cloud advected into the region at a height of 8 km between 25 km north and 25 km south of the VIL. These precipitating cirrus clouds are seen in the bottom half of Figure 1, the along wind scan. Virga fell approximately 2 km from these clouds before evaporating. Most of the cirrus clouds during this time period were seen north of the VIL.

For the second time period, 19:29 to 21:20 GMT, the cirrus clouds were more widespread. At 19:30 GMT, the cirrus clouds were similar to the earlier period with scattered thin cirrus clouds throughout most of the region. Again, these clouds often occurred in multiple layers. At 19:40 a precipitating cirrus cloud layer at a height of 8 km between 20 and 40 km to the south of the VIL moved into the region (Figure 7). This layer lasted for about one hour with virga falling 1 to 2 km below the precipitating layer. At 20:30 GMT, an extensive precipitating cirrus cloud deck advected into the region between 20 km south and 30 km north of the VIL (Figure 8). The precipitating layer occurred between heights 8.5 and 9.5 km with ice crystals falling to a height of 6 km. As the time period progressed, the cirrus cloud deck increased in optical thickness. Both to the north and south of the cirrus cloud deck multiple layers of thin cirrus clouds were seen. Also in Figure 8, the attenuation of the VIL signal can be seen. This loss of signal occurs between 7 km and 9 km further than 40 km north of the VIL and further than 30 km south of the VIL. The cirrus cloud layer at the tropopause was visible until 20:00 GMT.

3.3   Cloud Structure Summary

It has been shown that cirrus clouds are very complex in both the horizontal and vertical directions. These clouds are not homogeneous in either direction and can not be assumed so. Their complex structure needs to be viewed throughout a mesoscale sized volume to accurately describe the cirrus cloud spatial structure. These clouds have to be accurately described to understand the radiation balance in the Earth's atmosphere. The data set studied was only for a three hour time
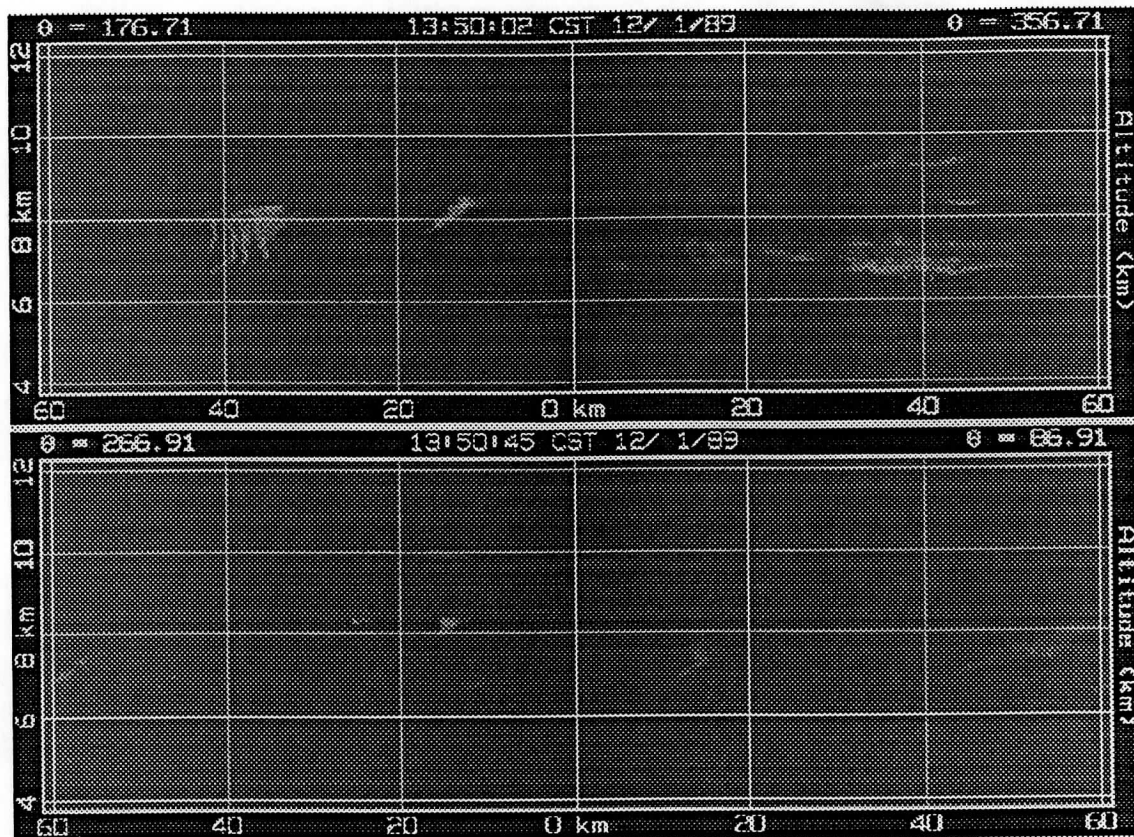
Figure 7: Typical cirrus clouds seen from 19:29 to 20:15 GMT. The x-axis is the distance from the VIL and the y-axis is altitude. The top picture is a cross wind scan, scanning from the North (357°) to the South (177°). The bottom picture is an along wind scan, scanning West (267°) to East (87°). The scan times are given in local time (CST). Both scans show the cirrus cloud variability.
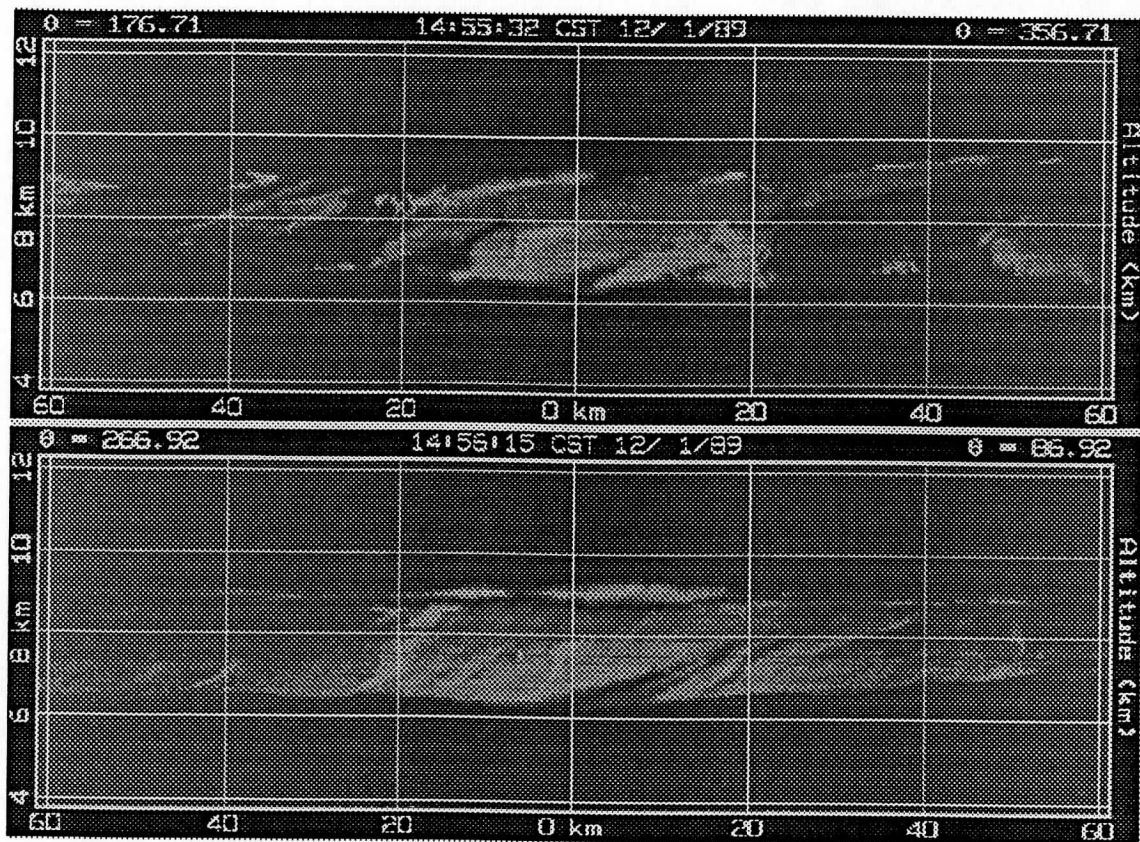
Figure 8: Same as Figure 7 but for the time period of 20:30 to 21:20 GMT. The precipitation from the cirrus clouds is easily seen in the along wind scan. Note the effects of attenuation at the longer slant paths in the bottom scan between 20 and 60 km West of the VIL near a height of 8km (also between 40 and 60 km East of the VIL at the same heights).

period. To better understand the general properties of the cirrus cloud spatial structure, a larger set of cirrus cloud data needs to be analyzed.

4 Cirrus Cloud Visible Optical Properties

Examination of the cirrus cloud structure has shown the advantages of a volume scanning system and the difficulties encountered by a vertically pointing instrument when attempting to describe the cirrus cloud spatial structure across a mesoscale volume. As shown by the simple radiative transfer calculations, the cirrus cloud optical properties play an important role in the radiation balance within the Earth-Atmosphere system. Like the cirrus cloud spatial structure, the cirrus cloud optical properties at visible and infrared wavelengths may vary significantly across a mesoscale volume. The visible optical depth influences the amount of solar radiation which passes through the cirrus clouds and reaches the lower levels of the Earth's atmosphere. The infrared optical depth moderates the amount of infrared radiation lost to space through these clouds. To understand the effects of cirrus clouds on the Earth's radiative budget, the cirrus cloud optical properties have to be known.

Previous attempts to determine the cirrus cloud visible optical depth, to compare to the cirrus cloud infrared optical depth, have been made using satellite based radiometers and ground based lidars. The calculations using satellite data could not independently determine the cirrus cloud visible optical properties since additional measurements of the cloud coverage and cloud types within each pixel were needed. These calculations also needed measurements of the reflectivity of the Earth's surface at the visible wavelengths for each pixel. Errors also occurred in the visible optical depth calculations due to poor calibrations of the visible channels. The visible channels were calibrated at the ground and the calibration has degraded over time. Ground based lidars have also been used to determine the cirrus cloud visible optical properties. The measurements by a vertically pointing

lidar are limited by the instrument viewing capability. These lidars only observe the cirrus clouds advected over their position producing biased results due to the cirrus cloud spatial variability and the possible preferential alignment of the cirrus clouds. A volume scanning ground based lidar needs to view a large enough volume of the atmosphere to remove pixel alignment errors associated with the direct comparison of the cirrus clouds viewed by the scanning lidar and the satellite radiometer (described in Section 5).

A new technique to calculate the cirrus cloud visible optical properties throughout a mesoscale volume is described in the following section. This method uses coincident cirrus cloud measurements from two ground based lidar systems, the VIL and the HSRL. The cirrus cloud visible aerosol backscatter cross sections calculated from the HSRL data are used to calibrate the VIL backscattered signal. The VIL cirrus cloud scans will then be used to extend the calibration to a mesoscale volume. This new calibration method, which uses data from two lidar systems, was attempted without previous knowledge of the errors associated with this calibration process.

4.1 Calibration Technique

The VIL and HSRL were aligned to view the same cirrus clouds during CRSPE. This alignment allowed the cirrus clouds to be used as a calibration target for the single channel VIL data. This calibration scheme was possible because the HSRL unambiguously determined the aerosol backscatter cross sections throughout the depth of the cirrus cloud as described in Section 2.1. The HSRL $\beta_a'(180, R)$ were directly correlated to the VIL backscattered signal for the simultaneously measured cirrus clouds. This was achieved using a cirrus cloud point comparison applied between the VIL backscattered signal and the HSRL $\beta_a'(180, R)$.

Before the VIL backscattered signal could be calibrated, corrections had to be made to the VIL data. The VIL backscattered signal which was at the limit of detectability of the receiver had to be removed from the data set. If these

system limited points were included in the VIL–HSRL comparison, an erroneous VIL signal calibration would result. The technique to remove the instrument limited data points is described in Appendix A. After the system limited points were removed from the data set, the VIL signal had to be corrected for angular dependencies in the data and/or possible temporal variations in the receiver (field of view changes or a change in gain of the avalanche photo–diode). This was accomplished by normalizing the VIL backscattered signal to a low level aerosol layer. This normalization technique, which required a spatially and temporally uniform aerosol layer to relate the VIL backscattered signal throughout time and space, is described in Appendix B.

After the corrections were made to the VIL data, a cirrus cloud point comparison between the VIL corrected raw signal and the HSRL $\beta'_a(180, R)$ was achieved. The VIL data which viewed the clouds over the HSRL were converted into an altitude verses time profile (RTI) simulating the HSRL data set. The HSRL RTI and VIL simulated RTI are shown in Figure 9. To create the VIL RTI, the backscattered signal was converted from spherical coordinates into cartesian coordinates. The VIL data was then averaged in distance around the HSRL site (24 km to the East of the VIL) to match the one minute averaging of the HSRL profiles. The average wind speed at the cirrus cloud heights was used with the averaging time of the HSRL data to determine the VIL averaging distance (~ 2 km). Errors between the positioning of the VIL and HSRL vertical profiles were caused by misalignments between the VIL along wind scan plane and the HSRL position (due to VIL scan angle errors). A cross correlation between the HSRL RTI and VIL RTI cloud points was calculated to find the best fit between the two profiles. The position of the peak in the cross correlation was compared to the position of the peak of an autocorrelation of the HSRL RTI data points. The difference between the peak positions for the two correlations revealed shifts between the two RTIs. For the 19:29-21:20 GMT time period, the VIL data was shifted one point (60 m) in the vertical and one point (one scan, 85 seconds or approximately 3 km) in

the horizontal compared to the HSRL data. The horizontal and vertical shifts between the data sets can result from: misalignment between the VIL scan direction and the wind direction, scan angle errors, and/or inconsistent time measurements between the two systems. The misalignment of the VIL scan direction in relation to the wind direction can lead to significant errors if there are large spatial variations in the cirrus cloud optical and structural properties. The associated errors result from the differences in the spatial averaging used to produce the HSRL and the VIL simulated vertical profiles. The HSRL data were averaged along the wind axis while the VIL data were averaged along the cirrus cloud scan axis; the two profiles were produced from different sections of the atmosphere. (The variations of the cirrus cloud particles and the associated errors are discussed at the end of this section.) Another problem can be the misalignment of the VIL along wind scan. Slight scan angle miscalculations will lead to relatively small distance errors. A 0.5^o error in the scan angles (azimuth and/or elevation) will lead to a 200 m error in scan position with regards to the HSRL profile. This can easily account for the vertical shift between the two data sets. A third problem resulted from differing time records between the two systems. The HSRL clock times were taken from the telephone. The times were given to the minute so they were $\pm$ 30 seconds. The telephone time was then stored in a Whole Sky Imager computer. Over a two week period, this clock drifted tens of seconds. Therefore the HSRL times are believed to be $\pm$ 1 minute. The VIL times were set from the radio every day resulting in less than 5 seconds of error. A 1 minute error between the two data sets is approximately a 2 km error in the cirrus cloud comparison. The shift of the VIL simulated RTI in relation to the HSRL RTI can be accounted for by these errors.

The resulting profiles, HSRL RTI and the shifted VIL simulated RTI, were compared on a point by point basis. The result of this comparison can be seen in Figure 10. A straight line of slope one which best fits the cirrus cloud backscatter
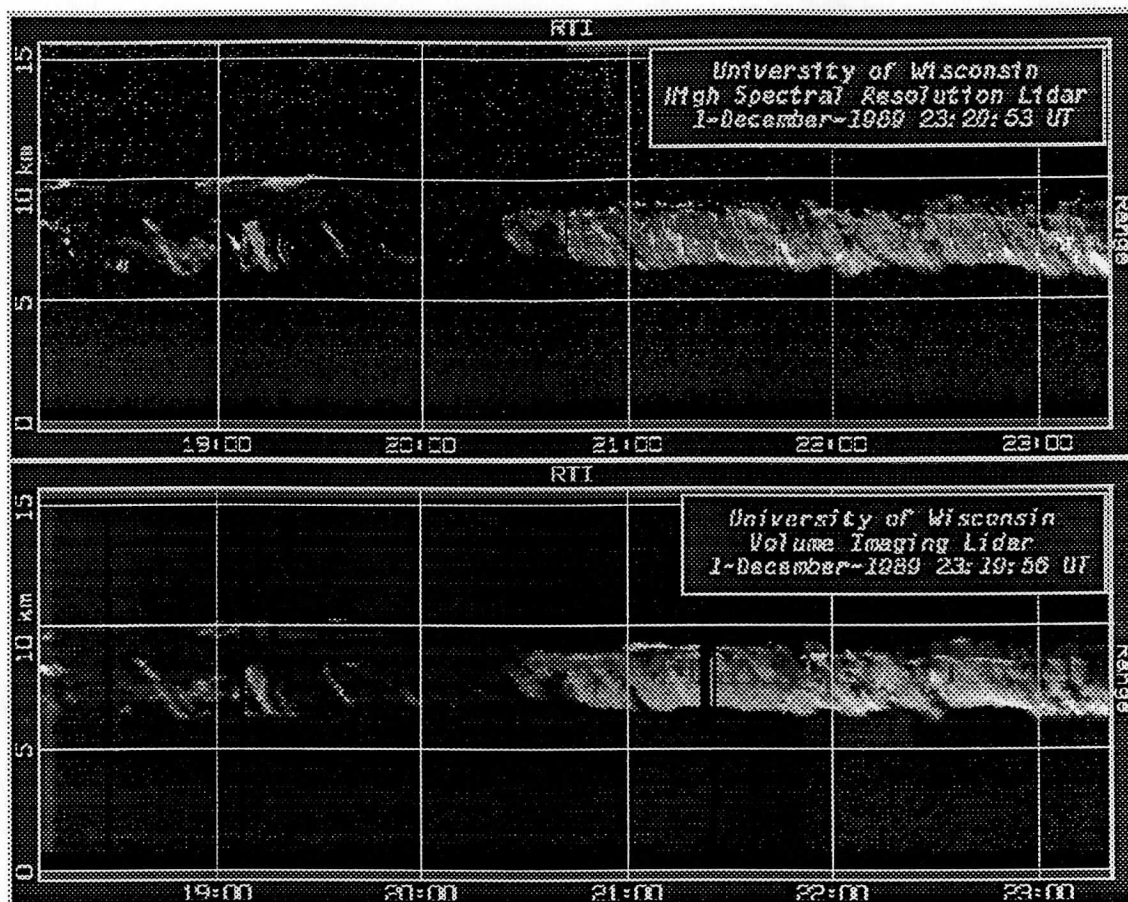
Figure 9: Comparison of cirrus clouds over Madison, Wisconsin from 18:08 to 23:20 GMT. The x-axis is time and the y-axis is altitude. The top picture is the HSRL RTI. The bottom picture is a VIL RTI 24 km East of the VIL over the HSRL. The VIL RTI is a synthetic RTI created from the VIL cirrus cloud scans to simulate the HSRL RTI. These two RTIs were used for the cirrus cloud point comparison between the two lidar systems.
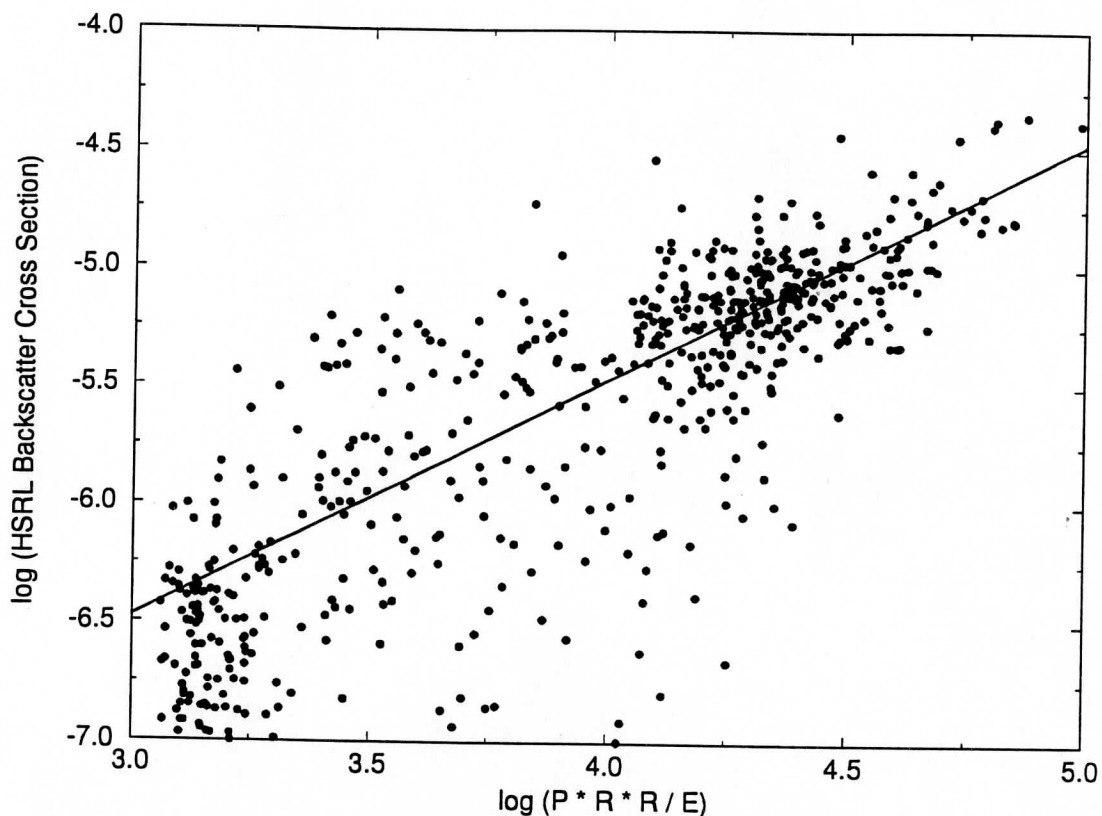
Figure 10: VIL–HSRL cirrus cloud data point comparison on December 1, 1989 from 19:29 to 21:20 GMT. The x-axis is the logarithm of the VIL range squared corrected, energy normalized signal. The y-axis is the logarithm of the HSRL aerosol backscatter cross sections. Since the VIL signal was not corrected for losses due to attenuation, only the bottom 1.5 km of the cirrus clouds was used in this comparison. The cirrus cloud threshold value used in Section 3 is located at 3.48. A straight line best fit to the cirrus cloud particles is also plotted.

data was also plotted. This best fit straight line was used to calibrate the VIL data; it related the VIL backscattered signal directly to the cirrus cloud aerosol backscatter cross sections per unit volume calculated from the HSRL data. A one-to-one relationship was expected because of the assumption that the scattering by the ice particles was independent of the wavelength of the incident visible radiation. In Figure 10, the VIL signal contains backscatter from both aerosols and molecules. For this comparison, the molecular backscatter at 1064 nm was small compared to backscatter from the cirrus cloud ice crystals and was neglected. (The molecular signal was about twenty times smaller than the background aerosol signal at the cirrus cloud heights for the 1064 nm wavelength radiation (see Section 4.2).) The signal from non-cirrus aerosols can be seen at the lower end of the plot in Figure 10. No VIL data had values less than 10^3 m^2 sr^{-1}. This was a result of the dynamic range of the VIL; data with values smaller than 10^3 m^2 sr^{-1} from a horizontal distance of 24 km could not be separated from the noise in the data system.

The VIL raw data in Figure 10 was not corrected for attenuation. To avoid attenuation problems in the initial calibration, the point comparison was only per-formed on the bottom 1.5 km of the cirrus clouds where attenuation was assumed negligible. This assumption would not be valid if the cirrus cloud was 1.5 km thick (with a cloud base at 6 km), had an average $\beta'_a(180, R)$ of $1 \cdot 10^{-4}$ m^{-1} sr^{-1}, and was viewed at an elevation angle of 4° out to 60 km. The optical depth would be 2 through the bottom 1.5 km of the cirrus clouds for this situation. For the cirrus clouds in this study, the average cirrus $\beta'_a(180, R)$ (from Figure 13) was $1 \cdot 10^{-5}$ m^{-1} sr^{-1}. This would give an optical depth of 0.2 only at far ranges (greater than 50 km) and low elevation angles. So for a distance of 24 km the as-sumption of negligible attenuation through the bottom 1.5 km of the cirrus clouds (in the vertical) was valid.

The bottom 1.5 km of the cirrus cloud seen by the VIL was calibrated using the HSRL $\beta'_a(180, R)$. The result of the calibration can be seen in Figure 11. Here the VIL signal at each point was transformed into a $\beta'_a(180)$. To calibrate the

VIL data throughout the depth of the cirrus clouds, corrections had to be made for signal loss due to attenuation. The technique to correct for the attenuation in the VIL data is described in Appendix C.

4.2   Calibration Results

The results of the calibrated, attenuation corrected VIL data between the heights of 6 to 9 km above the HSRL are seen in Figure 12. The point comparison between the HSRL $\beta_a'(180)$ and the calibrated VIL $\beta_a'(180)$ shows more scatter than the comparison for the data between the heights of 6 and 7.5 km. This was a result of the misalignment errors between the two profiles described earlier and the usage of a bulk aerosol backscatter phase function for the correction of the attenuation in the VIL signal.

The lowest $\beta_a'(180)$ detected by the VIL at a horizontal distance of 24 km was approximately $3 \cdot 10^{-7}$ m^{-1} sr^{-1} (-6.5 in Figure 12). The VIL data centered around a value of $5.0 \cdot 10^{-7}$ m^{-1} sr^{-1} (-6.3) corresponded to non-cirrus aerosol backscatter. Little correlation was expected in this range because of the wavelength dependence of the scattering at the two lidar wavelengths by the non-cirrus aerosols. The $\beta_a'(180)$ centered around $1.0 \cdot 10^{-5}$ m^{-1}sr^{-1} (-5.0) correspond to the backscatter by cirrus cloud ice particles. In Figure 12, the VIL calibrated $\beta_a'(180)$ are approximately 1.5 times greater than the HSRL $\beta_a'(180)$. This was a result of the VIL signal being corrected for multiple scattering while the HSRL signal was not. If a multiple scattering correction factor of 0.5 was included in the calculation of the HSRL $\beta_a'(180, R)$ (similar to the VIL multiple scattering correction), then $N_a(R)$ in Equation 10 would increase resulting in an increase in $\beta_a'(180, R)$.

The calibration of the VIL data was extended to the cross wind scans for the two time periods. This extension produced aerosol backscatter cross sections for the mesoscale volume at a resolution of 2-3 km parallel to the wind (a function of
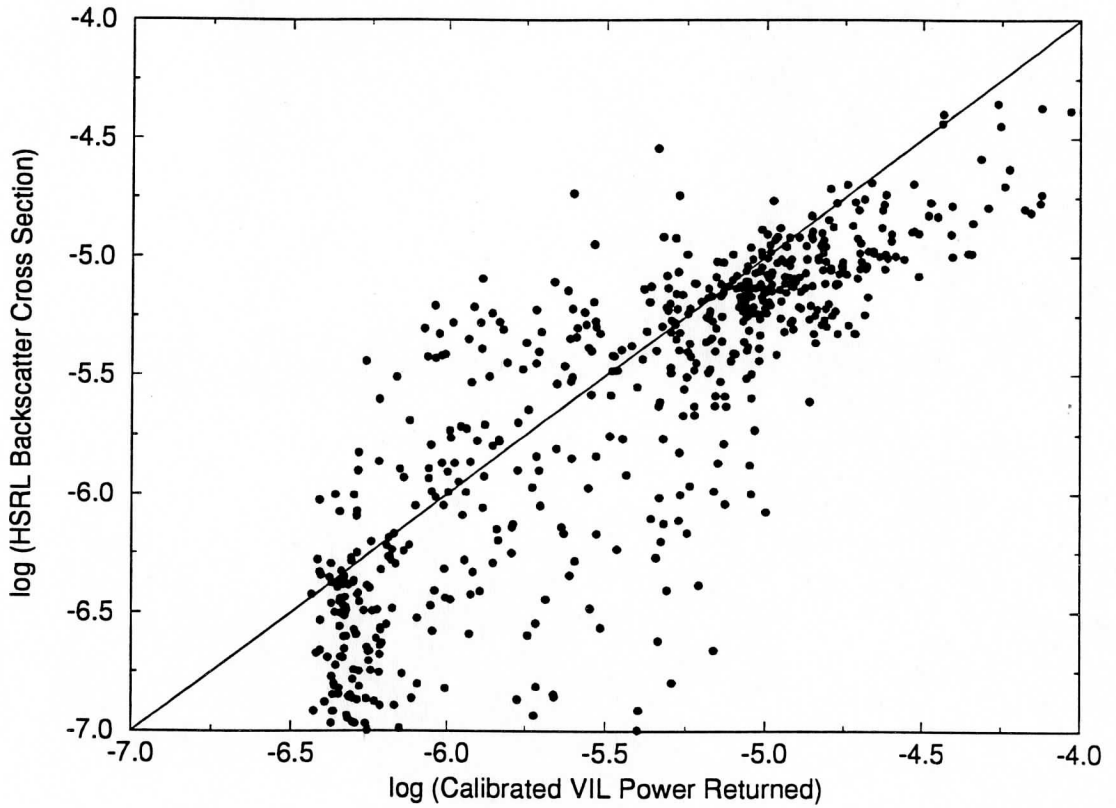
Figure 11: Same as Figure 10 except the calibrated VIL $\beta_a'(180, R)$ is compared to the HSRL $\beta_a'(180, R)$. A one to one line is plotted for reference.

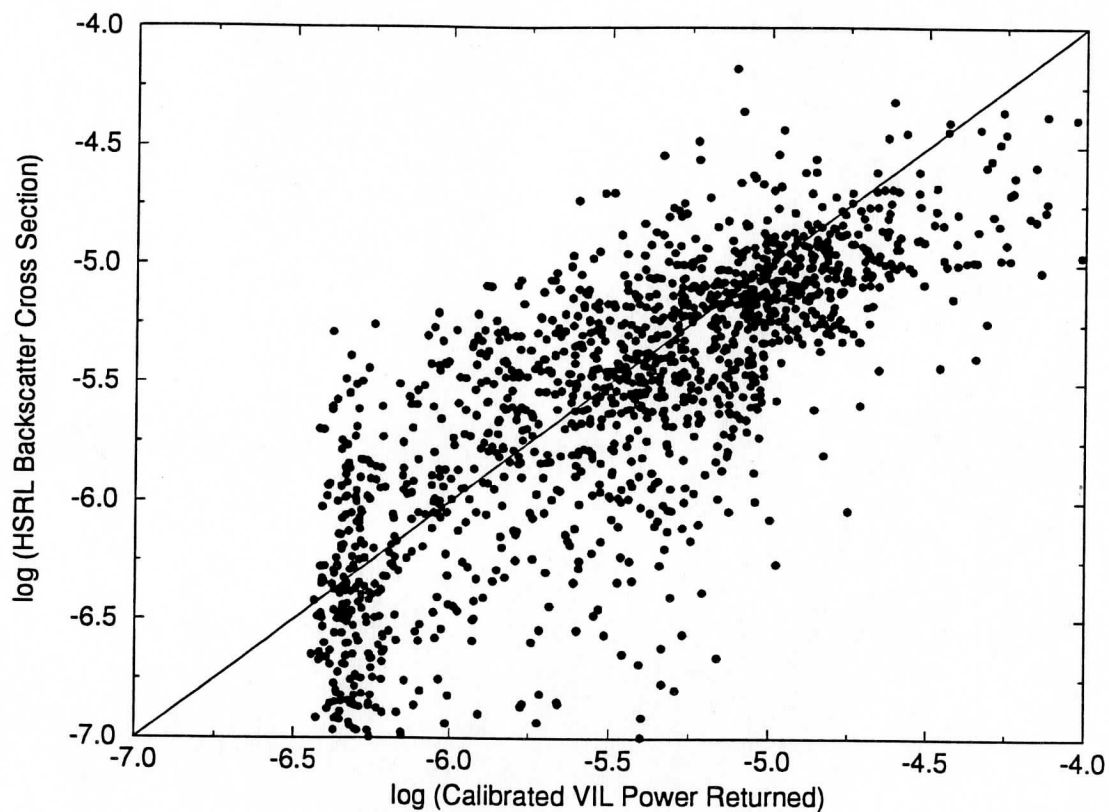Figure 12: VIL–HSRL cirrus cloud data point comparison on December 1, 1989 from 19:29 to 21:20 GMT. The x-axis is the logarithm of the calibrated VIL aerosol backscatter cross sections. The y-axis is the logarithm of the HSRL aerosol backscatter cross sections. The point comparison is for data between 6 km and 9 km in height, the depth of the cirrus cloud layer. A one to one line is plotted for reference.

the wind speed and the scanning rate of the VIL) and a resolution of 60 m in both the cross wind scan direction and the vertical. To determine whether the VIL calibrated $\beta_a'(180)$ for the mesoscale volume had a similar distribution to the VIL simulated RTI and HSRL RTI $\beta_a'(180)$ distributions, 50 point histograms of the data between the heights of 6 km and 11 km were computed. To create the VIL histograms, the molecular $\beta_m(180, R)$ was calculated using Equation 11 (for 1064 nm) and subtracted from the VIL calibrated backscattered signal. This allowed for the VIL and HSRL $\beta_a'(180)$ distributions for the atmospheric aerosols to be compared.

The resulting histograms are seen in Figure 13. A peak occurs in all three histograms near $8 \cdot 10^{-6}$ m^{-1}sr^{-1} (-5.2). This peak was associated with the cirrus ice particle $\beta_a'(180)$. In all three histograms, the range of $\beta_a'(180)$ for the ice crystals spanned from $1 \cdot 10^{-6}$ to $1 \cdot 10^{-4}$ m^{-1}sr^{-1}. The peak at the smaller $\beta_a'(180)$, which represents the non-cirrus aerosols, occurred near $1.5 \cdot 10^{-7}$ m^{-1} sr^{-1} for the HSRL RTI and the VIL data from the mesoscale volume. The non-cirrus aerosol peak for the VIL RTI, which occurred at $5.0 \cdot 10^{-7}$ m^{-1}sr^{-1}, shows the loss of signal at far ranges for the VIL. For $\beta_a'(180)$ below $3.8 \cdot 10^{-7}$ m^{-1}sr^{-1} (neglecting attenuation affects), the VIL receiver was not sensitive enough to detect the radiation backscattered from a horizontal distance of 24 km. The $\beta_a'(180)$ limit of detectability for a distance of 6 km can be seen in the histogram of the VIL data for the mesoscale volume. The smallest detectable $\beta_a'(180)$ was $1.25 \cdot 10^{-7}$ m^{-1}sr^{-1} (-6.8) as seen in Figure 13. Some HSRL $\beta_a'(180)$ were smaller than $1.0 \cdot 10^{-7}$ m^{-1}sr^{-1}. This was a result of incomplete separation between the aerosol and molecular channels for regions with small aerosol backscatter. This incomplete separation even led to some negative HSRL $\beta_a'(180)$ beneath the cirrus cloud layer. This problem has been removed in a new configuration of the HSRL (Piironen and Eloranta (1993)). Figure 13 also shows a relative minimum value for the $\beta_a'(180)$ near $1.0 \cdot 10^{-6}$ m^{-1}sr^{-1} for all three histograms. This relative minimum shows a clear separation between the background aerosol backscatter and the ice particle
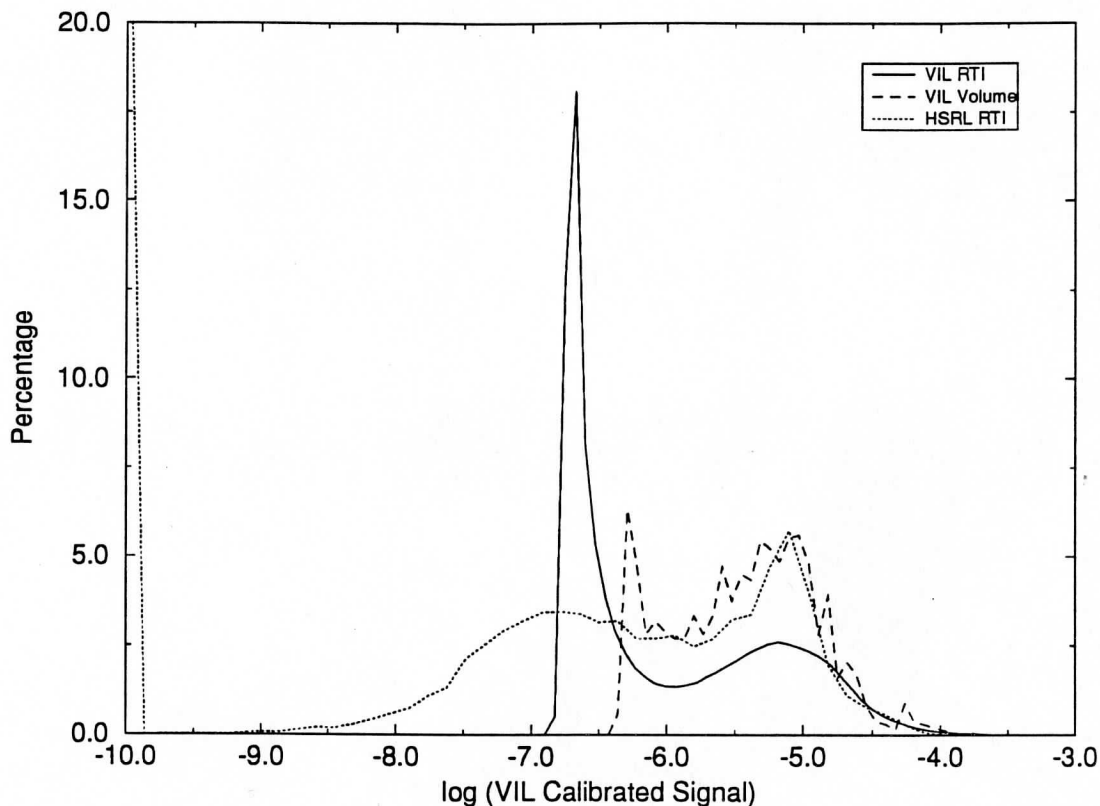
Figure 13: 50 point histograms of $\beta'_a(180)$ between heights of 6 km and 11 km from 19:29 to 21:20 GMT on December 1, 1989. The x-axis is the logarithm of $\beta'_a(180)$ and the y-axis is the percentage of points falling within each interval. Histograms of the HSRL $\beta'_a(180)$ (short dash), vertical profile of VIL $\beta'_a(180)$ over the HSRL position (24 km to the East of the VIL (solid line)), and the VIL $\beta'_a(180)$ throughout a mesoscale volume produced from consecutive VIL cross wind scans (long dash) are shown. The cirrus cloud threshold value used in Section 3 coincides with a value of $1.0 \cdot 10^{-6}$ m^{-1} sr^{-1}.

backscatter. This minimum value coincides with the threshold value used for the cirrus cloud determination in Section 3. At 1064 nm, the molecular backscatter cross section at a height of 6 km (calculated from the coincident rawinsonde density profile) was $6.44 \cdot 10^{-9}$ m^{-1}sr^{-1}. A typical aerosol backscatter cross section taken from the cirrus volume was $1.58 \cdot 10^{-7}$ m^{-1}sr^{-1}. By comparing these two values, it was determined that the signal backscattered by the background aerosols at a wavelength of 1064 μm was at least a factor of twenty greater than the molecular backscatter at the cirrus cloud heights during this experiment.

Although the peak at the ice crystal backscatter cross sections coincides for the three histograms, large variations are seen in the calibration plot between the VIL and the HSRL (Figure 12). The scatter seen in Figure 12 can result from variations in the $\frac{P_a(180,R)}{4\pi}$ throughout the cirrus mesoscale volume, misalignments between the two lidar systems, and/or signal noise. The $\frac{P_a(180,R)}{4\pi}$ are dependent on the shape (or type) of the ice crystals scattering the laser light. The $\frac{P_a(180,R)}{4\pi}$ for different types of ice crystals can change by 0.048 sr^{-1} as calculated by Takano and Liou (1989) (the values for the ice crystal $\frac{P_a(180,R)}{4\pi}$ varied between 0.037 and 0.085 sr^{-1}). If the cirrus $\frac{P_a(180,R)}{4\pi}$ changed significantly over the volume, then the actual $\beta_a'(180)$ will change along with the $\frac{P_a(180,R)}{4\pi}$ causing errors in the attenuation correction technique. A second cause for the errors in the calibration may be a result of the variations of the ice crystal $\beta_a'(180)$ across the cirrus clouds.

The variation of the $\beta_a'(180)$ for visible wavelengths within the cirrus clouds will give an estimate on the allowable error between the VIL scan plane and the HSRL position. If the cirrus particles vary significantly from point to point then the alignment of the VIL has to be precise. If, on the other hand, the $\beta_a'(180)$ for the cirrus particles vary slowly within the cloud, then small alignment errors will be acceptable. To determine the variation of the ice crystal $\beta_a'(180)$ between the cirrus cloud data points in the scanned mesoscale volume, autocorrelations of the along wind and cross wind cirrus scans were calculated.

During the first time period (18:07-19:24 GMT) scattered cirrus clouds occurred throughout the mesoscale volume. Along the wind, there was 95.6% correlation between cirrus cloud $\beta_a'(180)$ for data points separated by 100 meters in the horizontal. For a 200 meter horizontal separation, there was an 89.5% correlation between cirrus cloud points. At 500 meters, there was a 73.9% correlation and at a distance of 1000 meters, the correlation dropped to 55.9%. In the vertical, for data points separated by 60, 120 and 240 meters, there was an 82.9%, 58.9%, and a 31.4% correlation between the ice crystal $\beta_a'(180)$, respectively. The cirrus cloud $\beta_a'(180)$ correlations were also calculated for the VIL cross wind scans. For a 100 meter horizontal separation along the scan plane, there was a 94.6% correlation. At 200 meters, an 88.2%, at 500 meters, a 73.2% correlation, and at 1000 meters, a 54.6% correlation between the cirrus cloud $\beta_a'(180)$. In the vertical, at a 60 meter interval, there was a 79.0% correlation, 120 meters, a 49.1% correlation, and at 240 meter separation, a $\beta_a'(180)$ correlation of 29.3% was seen.

For this time period, the horizontal and vertical correlations were similar for the along and cross wind VIL scans. Good correlation existed for points separated by 100 to 200 meters. When the length of the correlation was extended to 500 and 1000 meters, the variation between data points became significant. The high correlation at 100 and 200 meter separations in the horizontal suggest that small azimuth angle alignment errors between the two systems can be tolerated. If the misalignments between the two profiles was as large as 1000 meters, then the resulting calibration would be very poor. In the vertical, only a maximum error of 60 m could be tolerated when generating a calibration for the VIL. The vertical cirrus cloud $\beta_a'(180)$ correlations changed more rapidly than the horizontal correlations. This was due to the vertical wind shear within the cirrus cloud. For the first time period, the larger separation lengths had correlations less than 50% for the cirrus ice crystal $\beta_a'(180)$. A calibration for the VIL could not be produced for larger separation lengths in the horizontal and the vertical due to the cirrus cloud $\beta_a'(180)$ variations.

For the second time period (19:29-21:20 GMT), the cirrus clouds were more

spatially uniform due to the presence of a cirrus cloud deck. For the along wind scan, at 100, 200, 500, and 1000 meter separations, correlations of 94.8%, 89.3%, 78.6%, and 67.9% were seen, respectively. In the vertical, at 60, 120, and 240 meter data point separations, correlations of 84.2%, 64.4%, and 45.3% were seen, respectively. For the cross wind scan, at 100, 200, 500, and 1000 meter separation between points, correlations of 95.2%, 89.3%, 75.6%, and 59.4% between the cloud data points existed. In the vertical, for 60 meter data point separation, an 82.1% correlation was seen while at 120 meters a 59.0% correlation occurred. At a 240 meter separation in the vertical, a correlation of 36.1% was detected. During this time period, the correlation values along the wind were higher than those in the cross wind scans for the larger distances between data points. This was a result of the widespread cirrus cloud deck over most of the region at this time which had an aspect ratio of 9:1.

For the VIL RTI simulating the HSRL RTI during the first time period, the correlation between cloud points was calculated. The correlation was computed along the wind direction with a separation between points (scans) in the horizontal of approximately 3 km and with a 60 meter data point separation in the vertical. In the horizontal, correlations of 76.3%, 48.2%, 18.1%, and 15.5% were seen at 1, 2, 5, and 10 scan separations (points). In the vertical, correlations of 89.2%, 71.0%, and 52.7% were seen at 60, 120, and 240 meter separations, respectively. For the second time period, correlations of 83.3%, 65.6%, 46.9%, and 36.1% were seen for 1, 2, 5, and 10 scan separations respectively. In the vertical, separations of 60, 120, and 240 meters resulted in 88.9%, 73.3%, and 55.1% correlations between the cirrus cloud aerosol backscatter cross sections, respectively. Higher correlations were seen in the vertical because these points were taken from a single cirrus cloud scan while the horizontal data points were taken from consecutive scans. The vertical correlations were similar to the previously calculated values as would be expected. There was very little correlation between the cirrus cloud particulate $\beta'_a(180)$ in the horizontal because of the large distances separating consecutive data points and the 2 km averaging along the scans to produce each profile.

The second time period had higher correlations in the horizontal than the first time period. This was a result of a widespread cirrus cloud deck which occurred during the second time period while the earlier period had scattered cirrus clouds throughout the region. The scattered cirrus clouds created a situation which made it difficult to produce a VIL RTI to match the HSRL RTI. The cirrus cloud deck on the other hand had more uniformity which allowed for greater scan angle errors between the two systems. Also, the VIL scan plane was more closely aligned with the wind direction at the cirrus cloud heights during the later period.

The cirrus cloud $\beta'_a(180)$ correlations revealed the types of error which would occur due to misalignments between the viewing positions of the two lidars. If large scan angle errors were present (greater than 1°), then the cirrus cloud point comparison between the HSRL RTI and the VIL simulated RTI would be poor due to the variation of the $\beta'_a(180)$ within the cirrus clouds. For acceptable calibration results, the VIL azimuth angle errors have to be less than 0.5^o and the elevation angle errors have to be less than 0.25^o.

For the two time periods, the cirrus cloud $\beta'_a(180)$ correlation values were similar but the calibration plots were not. The attempted calibration plot for the first time period (18:08 to 19:24 GMT) was very poor and as a result was not shown. The difference between the two time periods was the direction of the cirrus cloud advection and the widespread cirrus cloud deck throughout the later period. The clouds during the first time period were advected into the region from 283° while the clouds during the second time period came from 277° (on average). This difference of 6° between the wind direction and the VIL along wind scan direction result in point comparison errors in the calibration plot. The errors occurred when the VIL data was averaged along the scan plane to simulate the HSRL data (which was averaged along the wind direction). Since the VIL was averaged over the same distance as the HSRL profile (2 km), the offset between the VIL and HSRL data points at the end of the averaging length (1 km from each system) was 200 meters for the later time period and 300 meters for the early time period. The aerosol backscatter cross section correlation values across

the wind dropped approximately 14% at the end of the averaging distances for the given time periods. This reduction in correlation, along with the scattered cirrus clouds, made the production of a VIL calibration plot from the first time period data impossible. This shows the importance of either aligning the VIL along the wind or using smaller averaging times in determining the cirrus cloud visible optical properties from the HSRL.

5   Visible vs. Infrared Optical Depths

From Mie theory, in the limit of completely absorbing particles at 10.6 μm which are also large compared to visible wavelengths, the ratio of the visible scattering efficiency to the infrared absorption efficiency is expected to be 2:1. This ratio (Q_{vscat}/Q_{irabs}) has been used to describe the radiative properties of cirrus cloud ice crystals (Minnis (1991), p. 83). This efficiency ratio can also be written as the ratio of the visible scattering optical depth to the infrared absorption optical depth times an extinction efficiency ratio ($\frac{\tau_{vscat}Q_{vext}}{\tau_{irabs}Q_{irext}}$). Since the ice crystals were assumed to be large compared to both visible and infrared wavelengths, the extinction efficiency ratio was one and the optical depth of cirrus clouds at the two wavelengths are directly related. A relationship of this type allows for a simple parameterization for the cirrus cloud optical properties at the two wavelengths. Measurements of the optical depth at one wavelength allows for the optical properties of the cirrus clouds at the second wavelength to be calculated. Previous modeled ratios for cirrus cloud $\frac{Q_{vscat}}{Q_{irabs}}$ range from 1.8:1 to 4:1 (Minnis et al. (1993), p. 1281).

Few coincident measurements of the cirrus clouds optical depth at both infrared and visible wavelengths have been made to test the optical depth ratio determined from theory. Platt et al. (1980) made simultaneous measurements of cirrus clouds using a ground based lidar and a satellite based infrared radiometer. The ratio of the optical depths at the two wavelengths measured by Platt was less

than 2. The cirrus clouds were observed within a 10 km by 10 km volume using a single channel lidar. The visible optical depths were determined with the aid of a calculated backscatter to extinction ratio for the cirrus clouds. Measurements of cirrus cloud optical properties were also made during a FIRE IFO using ground based and satellite measurements. The mean ratio of the visible scattering optical depth to infrared absorption optical depth for the cirrus clouds observed during the IFO was 2.13 (Minnis et al. (1990)). The cirrus clouds were observed using a satellite based visible radiometer. The visible optical depths were calculated from these visible radiances using an iteration technique where the cloud albedo was linearly related to the cosine of the solar zenith angle. The cloud cover percent and cloud type within each pixel had to be known.

A method is described in this section to calculate the area averaged ratio of the $\frac{\tau_{vscat}}{\tau_{IRabs}}$ for cirrus clouds. This method used VIL data calibrated using the method described in Section 4 and the VAS 11 μm radiance measurements. The visible scattering optical depths were determined by integrating the VIL calibrated visible extinction cross sections (calculated using Equations 12 and 14) in distance along a ray from the GOES point of view. The infrared absorption optical depth was calculated from the VAS infrared emissivities which were determined using Equation 17. The mid-cloud height used in Equation 17 was determined by the VIL and the temperature at the mid-cloud height was measured with the rawinsonde.

The VAS on GOES imaged the atmosphere over Wisconsin once every half hour. To compare the visible and infrared optical depths, the VIL mesoscale volume was viewed from the position of the GOES satellite. This was possible because the VIL imaged the cirrus clouds throughout the mesoscale volume. The resulting VIL volume can be viewed from any direction because the $\beta_\epsilon(R')$ are known at each data point within the volume (calculated from the $\beta_a'(180, R')$ using the bulk backscatter phase function as described earlier). For an accurate lidar and satellite cirrus cloud comparison, the VIL cirrus cloud volume was broken into one hour time periods around each VAS picture. To match the cirrus clouds in the GOES infrared image to the picture created from the VIL data, the clouds

viewed by the VIL were shifted in position to the point where they would have occurred at the time of the VAS picture. The translation of the cirrus clouds was made under the assumptions that the cirrus clouds were advected at the speed of the wind at their heights and that the cirrus clouds did not change over a half hour period. The magnitude and direction of the shift was a result of the wind speed and direction at each cirrus cloud level and the time difference between the scan where the cirrus clouds occurred and the VIL scan at the time of the VAS snapshot.

To convert the VIL data within the volume into visible scattering optical depths, a ray tracing technique was used to integrate the VIL extinction cross sections between the satellite position and the ground. Rays were traced to the ground for each VIL area which had a resolution of 1.0 km by 1.0 km. The VIL extinction cross sections were integrated along each ray to determine the optical depth of the cirrus clouds for each visible pixel. The pixels were then averaged to create grids the size of the VAS infrared radiometer pixels, approximately a 10 km resolution above Madison, Wisconsin. The resulting averaged visible scattering optical depths were directly compared to the VAS infrared absorption optical depths calculated using the following equation (where ϵ_{ir} is calculated in Equation 17):

$$\tau_{ir} = -\ln(1 - \epsilon_{ir}). \tag{24}$$

The VAS infrared radiance satellite image was directly compared to the VIL visible optical depth simulated satellite image. The VIL visible optical depth image was position shifted to achieve the best cloud correlation between the two pictures to correct for cloud position errors in the VAS image due to satellite registration errors (this correlation was done by eye). A visible to infrared optical depth comparison was calculated for the pixels with high cloud cover percentages. The resulting comparison is shown in Figure 14. A line with a slope 2:1 is shown for reference. It should be noted that this optical depth comparison was achieved using an upper limit on $\beta'_a(180)$, not a limit on the attenuation correction factor.

This upper limit of $\beta_a'(180)$ did not remove a significant number of overcorrected data points which resulted from the attenuation correction. This leads to some overestimations of the visible optical depths especially at larger optical depths.

In Figure 14, the optical depth ratio from different cirrus cloud types is represented by different symbols. The clouds labeled as '1935 A' were thin nonprecipitating cirrus clouds which often occurred in overlapping layers. The ratio for these clouds was close to 2:1 with a slight tendency for the ratio to be less than 2:1. An example of these clouds is seen in Figure 7 between 20 and 50 km to the north. The second cloud type, '1935 B', was a band of precipitating cirrus clouds occurring between 30 and 40 km south of the VIL in Figure 7. These clouds also show an optical depth ratio close to 2:1. Both of these cloud types had visible optical depths less than 0.5. The remaining sets of clouds were thick precipitating cirrus clouds where the optical depths often became large. Extensive virga fell from these optically thick cirrus clouds to a height of 6 km. The cirrus clouds described as '2035 A' were precipitating bands occurring ahead of a large cirrus cloud deck. The optical depth ratio for these clouds tended to be less than 2:1. A fourth type of ice cloud was labeled '2035 D2'. These were clouds in the center of a large precipitating cirrus cloud deck. The optical depth ratios for these clouds also tended to be less than 2:1. Some of the cirrus clouds were too optically thick for the VIL signal to penetrate at longer slant paths. This led to smaller than expected visible optical depths which resulted in a ratio of less than 2:1. The last group of cirrus were labeled '2035 D1'. This group consisted of three cirrus cloud cross wind scans within the large precipitating cloud deck which had vertically thin layers of high backscatter. The optical depth ratios for these clouds ranged from 2:1 to 3:1. Optical depth ratios greater than 2:1 can result from: specular reflection in the VIL data, pixel misalignments between the two images, incorrect averaging of the VIL data, instability in the VIL attenuation correction procedure, and smaller than expected scattering particles.

Specular reflection in the three cross wind scans could not have caused the
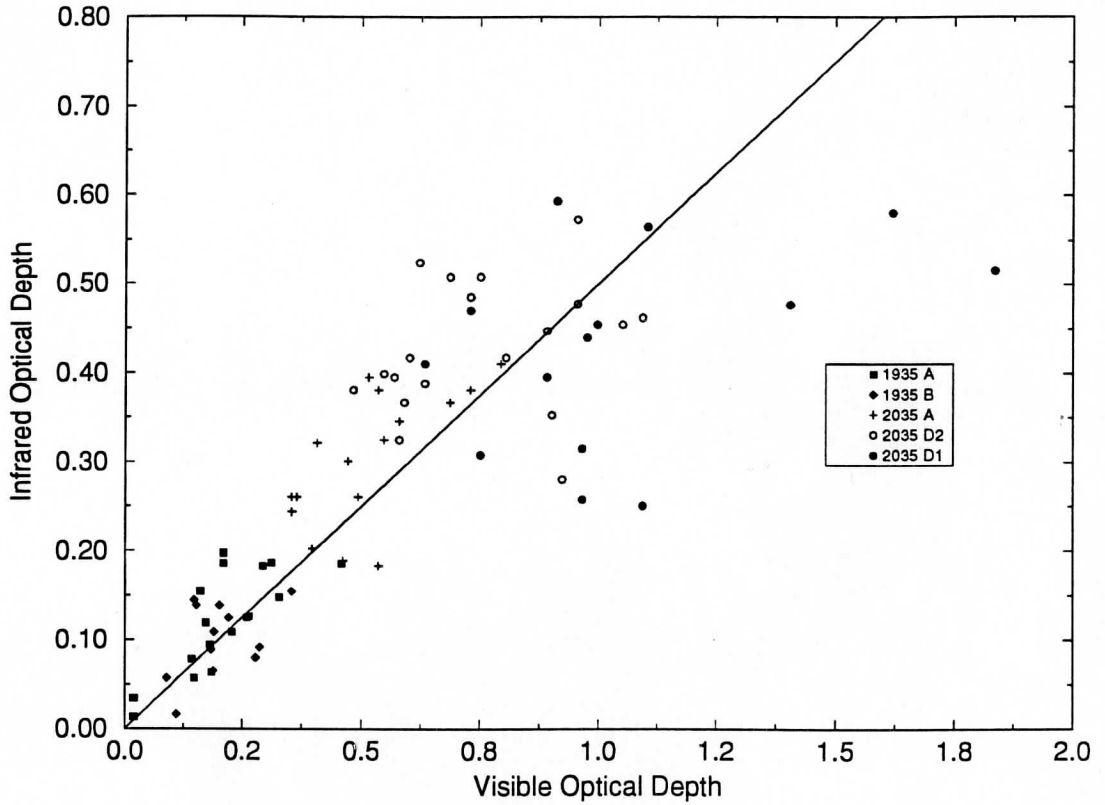
Figure 14: VIL visible scattering optical depths verses VAS infrared absorption optical depths for the same cirrus cloud pixels from 19:29 to 21:20 GMT on December 1, 1989. The x-axis is the VIL visible scattering optical depths. The y-axis is the VAS infrared absorption optical depths. The different symbols represent different cirrus cloud types described in the text.

thin regions of high backscatter. The increased backscatter layer extended over a horizontal range of 40 km. The ice crystal orientation would have had to change with the VIL scan angle to cause specular reflection for the whole range (which was highly unlikely). A second possible error was the allocation of the cirrus clouds into the different cirrus cloud pixels. This can result in an increase or a decrease in the optical depth ratio depending on which satellite pixel the cirrus clouds fell. The magnitude of these allocation errors are currently under investigation. Another cause for an optical depth ratio greater than 2:1 could be the result of the averaging technique to produce the visible optical depths at the 10 km scale. For each satellite pixel, the average infrared radiance was measured. This was converted into an effective temperature which was then used to calculate the infrared optical depth. The visible optical depths were produced at a 1 km scale by averaging the extinction cross sections at each level and then integrating them with height. The 1 km visible optical depth pixels were then averaged together to produce a 10 km scale image. Since the effect of the optical depth on the transmitted radiation was nonlinear, the VIL extinction cross sections should have been averaged over the 10 km infrared image. A probable error in the optical depth comparison was the instability in the VIL attenuation correction technique. This effect only becomes important for the clouds with large optical depths since the corrections at the smaller optical depths were minimal. One last error could result if the scatterers were not large compare to both the 11 μm and 0.5 μm radiation. If the particles were spherical and consisted of ice, then the scatterers with radii between 0.1 μm and 4 μm would cause an optical depth ratio greater than 2:1.

Some other errors associated with this visible to infrared optical depth comparison are scattering of the infrared wavelength radiation by the cirrus cloud ice particles (especially at larger infrared optical depths), the assumption that the upwelling infrared radiation has a T^4 dependence, and the attenuation of the VIL signal through thick cirrus such that the VIL signal does not penetrate through the clouds. If infrared radiation was scattered by the cirrus cloud or reflected from the

cloud base, less infrared radiation from beneath the cloud would reach the satellite radiometer. This would reduce the radiance detected by the radiometer which would result in a calculated cirrus cloud emissivity which would be larger than the actual cirrus cloud infrared emissivity. The higher cloud emissivity would result in a larger optical depth which would result in an optical depth ratio smaller than 2:1. The assumption that the upwelling infrared radiation has a T^4 dependence will result in an error in the calculated emissivities of approximately 3%. Another problem was the incomplete penetration of the cirrus cloud by the VIL. For the VIL, total penetration of the cirrus clouds is needed to make accurate calculations of the visible scattering optical depths across the mesoscale volume. Incomplete penetration would cause an underestimation in the thickness of the cirrus clouds which would result in underestimations of the visible scattering optical depths. This underestimation of the cloud depth would also lower the optical depth ratio.

When comparing the VIL optical depth image to the VAS infrared radiance image, large variations were seen in the visible image while very little variation between pixels was seen in the infrared satellite image. This relative uniformity in the satellite infrared image was a result of the large area covered by each pixel and the smearing that occurred between pixels. This pixel smearing was due to the response rate of the infrared detector and the sampling rate of the VAS. Also, the calculation of the emissivity was strongly dependent on the choice of surface temperature and mid-cloud temperature as seen in Equation 17. A lower haze layer or subvisible cirrus clouds which were undetected in the satellite image would cause lower than expected surface temperatures which would decrease the cirrus cloud emissivity.

The technique described here to compare the visible scattering optical depth to the infrared absorption optical depth removes ambiguities associated with the previous visible to infrared optical depth comparison. The cirrus clouds were compared on the same scale removing horizontal homogeneity assumptions. The cirrus clouds were viewed from the same direction at the same resolution removing angular viewing effects. Since both systems viewed the cirrus cloud horizontal

structure, the pixel alignment between the two images could be done. The cirrus cloud base, top, and mid-cloud height were determined for each cloud pixel from the VIL data. This removed the uncertainty of the mid-cloud height in determining the mid-cloud temperature used to calculate the cirrus infrared emissivities. For the time periods studied here, the VIL was able to detect subvisible cirrus clouds. These clouds, not seen in the infrared channels, would have been ignored in the determination of a surface temperature from a clear pixel which was used in the calculation of the cirrus cloud infrared emissivities. This removed some of the surface temperature uncertainties. At visible wavelengths, the ground albedo was needed for cirrus cloud albedo calculations from satellite based visible radiometers. The calculation of the visible optical depth from the VIL did not need ground albedo values because the visible optical depth of the cirrus was directly determined from the integration of the cirrus visible extinction cross sections along the line of sight of GOES. The bulk cirrus cloud backscatter phase function used by the VIL was determined from the HSRL enabling the technique to be self contained.

Although it was not done in this study, the level of the cloud where maximum scattering occurs can be determined by integrating the VIL extinction cross section along a viewing angle using the ray tracing technique. The height can be compared to the mid-cloud height to calculate the errors associated with the usage of the mid-cloud temperature in determining the cirrus infrared emissivity and optical depth.

6   Conclusion

Cirrus clouds were viewed using the University of Wisconsin Volume Imaging Lidar, University of Wisconsin High Spectral Resolution Lidar, and the VAS radiometer situated on GOES. The VIL imaged the cirrus clouds within a mesoscale volume. The HSRL measured the visible scattering properties of the cirrus clouds.

The VAS radiance measurements were used to calculate the infrared absorption properties for the cirrus clouds.

The backscattered radiation detected by the VIL was used to determine the horizontal and vertical structure of the cirrus clouds. The presence of cirrus clouds was determined by choosing a threshold value from a histogram of the VIL backscattered signal between heights of 6 and 11 km. The backscattered radiation in each VIL profile was compared to the threshold value to determine cirrus cloud cover percentages and structure functions. The cirrus cloud cover percentages ranged from 54.7% to 100% for simulated vertical profiles across the wind created from the VIL cross wind scans. For the two time periods studied, the area averaged cirrus cloud cover percentages were 81.5% and 76.8%. Differences in the average cloud cover were seen between the VIL area measurements and HSRL vertical profiles. The maximum cloud cover difference of 45.3% between two VIL RTIs during the first time period was used as a cirrus cloud cover error to estimate a resulting change in the incoming solar radiation. This cloud cover error, along with an average cirrus cloud optical depth of 0.257, resulted in an estimated change in the direct solar flux of 58.18 W m^{-2} seen at the surface of the Earth. For the second time period, a cloud cover difference of 8.9% between the VIL and HSRL, associated with a cloud optical depth of 0.428, resulted in a 12.36 W m^{-2} difference in direct solar flux seen at the surface of the Earth. The errors due to the incorrect cirrus cloud cover would dominate the increase in the planetary effective temperature resulting from the doubling of CO_2, especially in the case of spatially scattered, optically thin cirrus clouds. This implies that the variability of the cirrus clouds throughout a mesoscale volume has to be measured to understand the effects of these clouds on the Earth's radiation balance. Sampling errors associated with point measurements make them poor indicators of the cirrus cloud area averaged values.

The cirrus cloud horizontal and vertical structure was also examined. Structure functions were used to determine the cirrus cloud length, width, and the separation between clouds. The cirrus cloud average length along the wind was 130 km and its

length across the wind averaged 14 km. The average distance between clouds along the wind was 273 km while across the wind it was 24 km. In this experiment, the cirrus clouds were typically aligned along the wind direction with an aspect ratio of approximately 9:1. Preferential alignment of cirrus clouds implies that point measurements which rely on cloud advection may not even detect cirrus clouds if large variations exist across the wind. Examination of the vertical cloud structure showed many instances of multi-layered and/or precipitating cirrus clouds. The complexity of the vertical structure shows the dependence of cloud formation on the dynamical situation in the atmosphere.

A method was described to calculate the cirrus cloud visible optical properties across a mesoscale volume. This was possible because an experiment was run where the VIL along wind scan plane crossed over the HSRL position resulting in coincident cirrus clouds measurements. The HSRL cirrus cloud aerosol backscatter cross sections were used to directly calibrate the VIL backscattered signal. A point comparison was made for the HSRL aerosol backscatter cross sections and the VIL data (which was normalized to a low level aerosol layer to remove angular dependencies). This initial comparison was computed for the signal backscattered from the bottom 1.5 km of the cirrus clouds where it was assumed that the attenuation in the VIL signal was negligible. A best fit straight line was used to calibrate the VIL backscattered signal into aerosol backscatter cross sections per unit volume. The calibrated VIL signal was then attenuation corrected using a forward integration of the single channel lidar equation. To forward integrate the lidar equation, extinction cross sections at each data point and a multiple scattering correction factor were needed for the VIL data. Extinction cross sections were created from the VIL calibrated aerosol backscatter cross sections using a single aerosol backscatter phase function for the whole volume calculated from the HSRL data (assuming negligible molecular extinction within the cirrus cloud compared to the aerosol extinction at 1064 nm). A multiple scattering correction factor of 0.5 was used to correct the backscattered signal to account for one half of the original scattered light being diffracted by the ice particles and staying within the

receiver field of view. After the VIL signal was attenuation corrected, the result-ing calibrated VIL cirrus cloud aerosol backscatter cross sections were compared to the original HSRL aerosol backscatter cross sections. An adequate correlation resulted between the two sets of aerosol backscatter cross sections. The largest errors in the calibration technique resulted from VIL scan angle errors leading to misalignments between the two vertical profiles, misalignments between the VIL scan direction and the wind direction, and the usage of a bulk aerosol backscatter phase function in the VIL attenuation correction technique. The alignment of the VIL scan and the HSRL vertical profile was critical since the calibration technique was dependent upon both system viewing the same cirrus cloud.

The calibration technique was used to convert the VIL signal in both scan directions into aerosol backscatter cross sections per unit volume. The calibrated cross wind VIL data was used to calculate the visible scattering optical depth of the cirrus clouds within the mesoscale volume assuming no changes in the cirrus clouds as they were advected by the wind (over a half hour period). The visible optical depths were calculated by integrating the VIL cirrus cloud extinction cross sections along a path through the VIL observed volume traced by a ray from the position of the GOES satellite. This allowed for a direct comparison of the VIL visible scattering optical depths and VAS infrared absorption optical depths. The ratio of the VIL visible scattering optical depth to the VAS infrared absorption optical depth was approximately 2:1 (especially for thin cirrus clouds) although variations did occur. The 2:1 ratio value agrees with previous measurements by Minnis (1990). When making this optical depth comparison, the cirrus clouds detected by the VIL had to be correctly allocated into the different pixels to enable an accurate comparison with the infrared image. This process was hampered by the lack of variation in the infrared image compared to the visible cirrus cloud image.

The technique to compare the visible scattering to infrared absorption optical depths can also be used to compare the cloud cover determined from the VIL to the cloud cover calculated from the satellite infrared radiometer data using the

CO_2 slicing technique. This comparison would be used to test the accuracy of the satellite based cirrus cloud climatologies. The cirrus cloud albedo and mid-cloud height calculations from satellite based radiometers can also be tested. The level of maximum scattering within a cirrus cloud can also be determined and compared with the cirrus mid-cloud heights throughout the mesoscale volume. Although these comparisons are not encompassed in this thesis they can easily be accomplished with the tools available.

This first attempt at a calibration of the VIL backscattered signal by the HSRL aerosol backscatter cross sections shows promise. Some of the inherent problems in this technique were revealed. Improvements are being made to both the VIL and the HSRL. This will result in more accurate measurements which will lead to a better understanding of the cirrus cloud optical and structural properties. The cirrus cloud detection technique and the VIL calibration technique should be attempted on a large cirrus cloud data set to achieve a statistical representation of the cirrus cloud optical and structural properties.

A   Removal of System Limited Data Points

To correctly calibrate the VIL data, the system limited data points had to be removed from the data set. At far ranges the backscattered radiation can not be separated from the system noise because the VIL signal decreases due to the range squared dependence and attenuation. When the VIL raw data is corrected for the range squared dependence, the places where the VIL signal increases monotonically as a function of the range is where the signal could not be separated from the noise as seen in Figure 15. This limit of detectability occurs where the VIL signal starts to increase with range around bin 250. The large increase in the signal around the range bin 500 was the result of radiation backscattered from a cirrus cloud.

To remove the noise dominated points, the points where the raw signal was within the noise regime had to be determined. At far ranges, the raw backscattered signal becomes linear with range when the backscattered power is plotted on a natural log scale. This was a result of both the attenuation of the transmitted pulse in the atmosphere and the range squared decrease of the signal. Shot noise occurs along with the raw signal. If the shot noise was random, as expected, then the noise should occur as a Gaussian distribution about the raw data. This would not affect the slope of the VIL data with range in Figure 15. So, if the VIL raw data was sorted according to their magnitudes and replotted on a log-linear plot, then the signal which was small and could not be separated from the noise would appear as a straight line at the lower signal magnitudes (Figure 16).

This process was applied to each VIL raw profile where the VIL backscatter signal was sorted according to their magnitudes. The sorted values were approximated using a straight line median fit. The straight line median fit was first applied to the whole sorted profile. The points occurring above the fit had large signal backscatter and were remove from the sorted set. The remaining sorted points were then refitted using a straight line median fit. After a number of successive fits, where a chosen threshold was met, the remaining points consisted

only of the small signal values which could not be separated from the noise (they appear as a straight line in Figure 16). These noise points were discarded from the original data set. For the shot used in Figure 15 and Figure 16, over one half of the data points had to be discarded. The remaining data points are the signal backscattered by aerosols and molecules in the atmosphere.
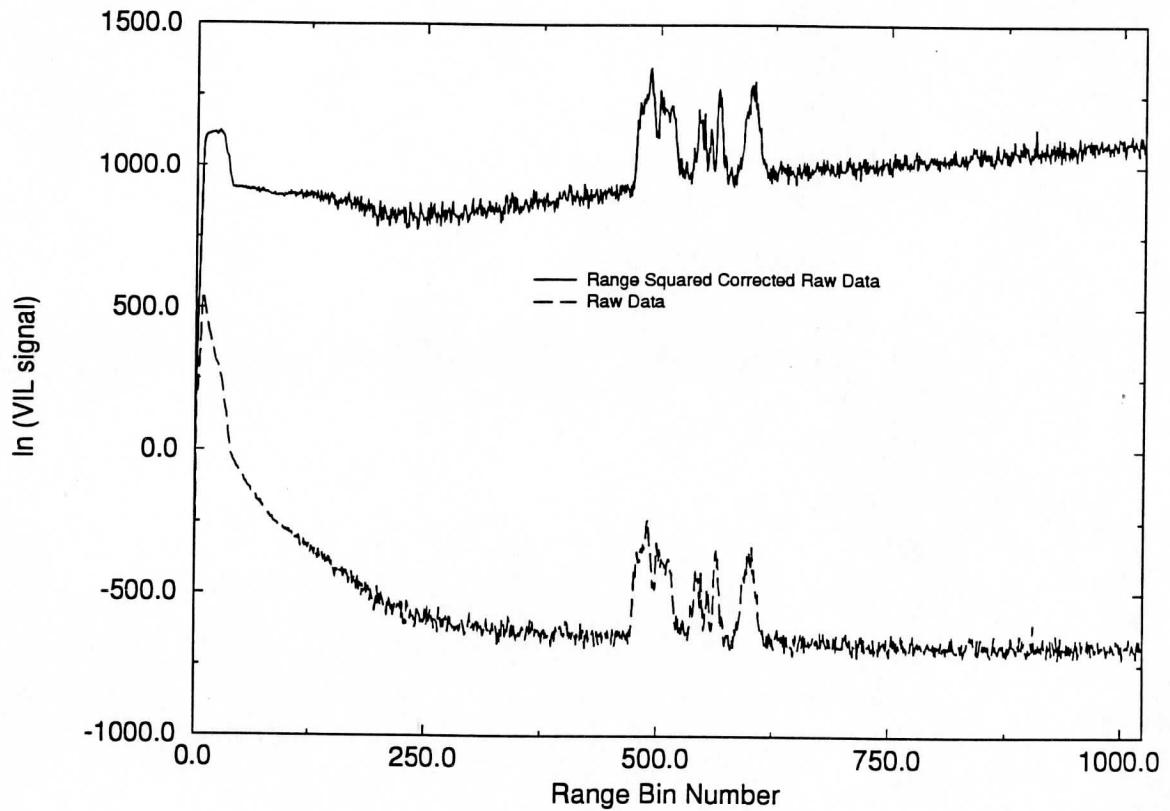
Figure 15: Removal of the noise points from the VIL raw data. The x-axis is the range bin number and the y-axis is $128 \cdot \ln (P / E)$ for the raw data and $128 \cdot \ln (P * R * R / E)$ for the range squared corrected raw data. The solid line is the range squared corrected VIL profile. The long dashed line is the VIL raw data profile.
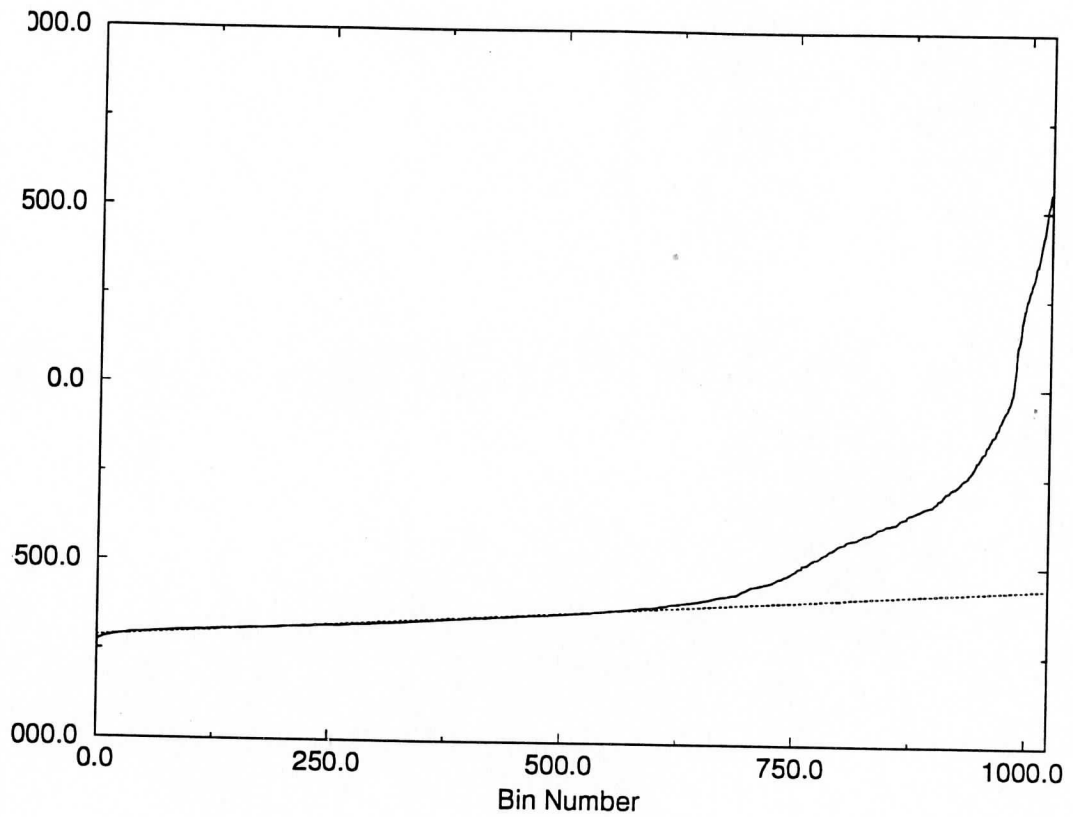
re 16: Removal of the noise points from the VIL raw data. The x-axis is the
ed bin number. The y-axis is $128 \cdot \ln (P / E)$. The solid line is sorted VIL
data (sorted according to magnitudes). The dashed line is the straight line
ian best fit to the sorted noise points.

B Data Normalization

Since the VIL mechanical axis was not aligned with its optical axis during this experiment, alignment errors were a problem for the VIL. The VIL signal varied when the system mirrors were scanned in angle as a result of partial blocking of the transmitted beam (an example is baffle blocking of the transmitted pulse). Other signal variations can also result from changes in the gain of the avalanche photo–diode over time and/or field of view changes in the receiver. To remove these dependence, each VIL scan was normalized to a low level aerosol layer situated between 1 km and 2 km above the ground. Only backscattered signal falling within a bounded aerosol region were used in the data normalization. The region was bounded by a minimum and maximum height along with a minimum and maximum distance from the VIL. The minimum and maximum heights were determined by the size of the aerosol layer. The minimum range from the VIL was determined by the extent of the system overlap regime. A maximum range of 10 km was chosen to stay well above the minimum detectable signal for the VIL. The median backscattered signal from the bounded aerosol layer for each lidar profile was set equal to the median backscattered signal in the normalization regime. This normalization technique removed both the time and angular dependence of the cirrus clouds scans with the assumption that the aerosol layer did not change in time. If the aerosol layer did not have temporal and spatial uniformity, errors would result from the normalization process. Nonuniformities would cause variations in the cirrus cloud backscatter which are the result of data processing and not cirrus cloud variability. The aerosol layer used for the VIL data normalization was detected by the HSRL and appeared uniform in time. Additional errors can also result if too much outgoing signal was blocked before it left the transmitter. When this occurred, the radiation backscattered from the atmosphere was too small to be separated from the noise. These system limited data points were removed from the data set as described in Appendix A.

C Attenuation Correction

To correct for the attenuation in the VIL signal, the optical depth between the VIL and each point in the profile has to be known (Equation 1). To determine the optical depth between the VIL and each data point, the extinction cross section at each point has to be determined. Since the VIL data was converted into aerosol backscatter cross sections, these values were used to calculate the extinction cross sections. The aerosol backscatter cross sections were first converted into aerosol scattering cross sections using Equation 2 assuming no absorption and additional knowledge of a bulk $\frac{P_a(180,R)}{4\pi}$ for the mesoscale volume. The average bulk $\frac{P_a(180,R)}{4\pi}$ calculated with the HSRL was used as the bulk $\frac{P_a(180,R)}{4\pi}$ for the mesoscale volume. Since no absorption at visible wavelengths by the cirrus ice crystals was assumed, Equation 14 relates the aerosol scattering cross sections to the extinction cross sections. A forward integration was performed on the resulting extinction cross sections to determine the attenuation between the VIL and each data point. The attenuation to each point was used to correct the existing VIL $\beta_a'(180,R)$ for signal loss. In this analysis, a multiple scattering correction was included. The attenuation along each profile was corrected by a multiple scattering factor of 0.5 which decreased the attenuation by a factor of 2 (Eloranta and Shipley (1982)). This correction factor was a result of half of the light attenuated by the cirrus cloud ice particles being diffracted in the forward direction. This diffraction peak stayed close to the initial beam and further scattering of this light by other particles resulted in greater backscatter at the receiver.

The bulk $\frac{P_a(180,R)}{4\pi}$ for cirrus cloud particles was calculated by the HSRL for each cirrus profile. These bulk $\frac{P_a(180,R)}{4\pi}$ were averaged over the 3 hour time period resulting in a $\frac{P_a(180,R)}{4\pi}$ of 0.0499 sr^{-1}. This value fell within the expected range of $\frac{P_a(180,R)}{4\pi}$ as described by Takano and Liou (1989). Their results give values of $\frac{P_a(180,R)}{4\pi}$ for thin plates (0.025 sr^{-1}), ice columns (0.038 sr^{-1}), and thick plates (0.087 sr^{-1}). (Plates were detected at the tropopause as noted by the specular reflection described previously.) This average $\frac{P_a(180,R)}{4\pi}$ was used to correct all of

the VIL data for attenuation.

The method of a forward integration of the backscattered signal was first used to correct radar backscatter for attenuation. Hitschfeld and Bordan (1954) were one of the first to test the forward integration method. Klett (1981) showed the instability of this forward integration for large optical depths. In this study, if the one way optical depth of the cirrus cloud along each VIL profile became greater than 0.7, then the attenuation correction at further ranges (or larger optical depths) was considered to be unstable. This choice in the one way visible optical depth was chosen on the assumption of a 10% error in the VIL aerosol backscatter cross sections. The attenuation correction (using an optical depth of 0.7) of the data with a 10% error would result in a 40% error in the attenuation corrected signal.

References

[1] Ackerman, Steve A., Eloranta, Ed W., Grund, Chris J., Knuteson, Robert O., Revercomb, Henry E., Smith, William L., and Donald P. Wylie (1993): University of Wisconsin Cirrus Remote Sensing Pilot Experiment. *Bulletin of the American Meteorological Society*, **74**, p. 1041–1049.

[2] Barton, I. J. (1983): Upper Level Cloud Climatology from an Orbiting Satellite. *Journal of the Atmospheric Sciences*, **34**, p. 758–765.

[3] Cess, R. D. et al. (1990): Intercomparison and Interpretation of Climate Feedback Processes in 19 Atmospheric General Circulation Models. *Journal of Geophysical Research*, **95(D10)**, p. 16601–16615.

[4] Dorsey, N. Ernest (1940): "Properties of Ordinary Water–Substance." Reinhold Publishing Corporation, New York.

[5] Eloranta, E. W. and S. T. Shipley (1982): A Solution for Multiple Scattering. "Atmospheric Aerosols: Their Formation, Optical Properties, and Effects." Spectrum Press, Hampton, Va, p. 227–237.

[6] Grund, Christian John (1987): Measurement of Cirrus Cloud Optical Properties by High Spectral Resolution Lidar. Ph.D Thesis, University of Wisconsin–Madison, 92 pp.

[7] Klett, James D. (1981): Stable Analytical Inversion Solution for Processing Lidar Returns. *Applied Optics*, **20**, p. 211–220.

[8] Liou, Kuo-Nan (1980): "An Introduction to Atmospheric Radiation." Academic Press, San Diego, California.

[9] Liou, Kuo-Nan (1986): Review: Influence of Cirrus Clouds on Weather and Climate Processes: A Global Perspective. *Monthly Weather Review*, **114**,

p. 1167–1199.

[10] London, J. (1957): A Study of the Atmospheric Heat Balance. Final Rep., Contract AF19(122)–165. Dept. of Meteorology and Oceanography, New York University, 99 pp. [AST1A 117227, Air Force Geophysics Laboratory, Hanscom AFB, Mass 01730.]

[11] Minnis, Patrick, Young, David F., Sassen, Kenneth, Alvarez, Joseph M., and Christian J. Grund (1990): The 27–28 October 1986 FIRE IFO Cirrus Case Study: Cirrus Parameter Relationships Derived from Satellite and Lidar Data. *Monthly Weather Review*, **118**, p. 2402–2425.

[12] Minnis, Patrick (1991): Inference of Cirrus Cloud Properties from Satellite–Observed Visible and Infrared Radiances. Ph.D. Thesis, Department of Meteorology, University of Utah, 161 pp.

[13] Minnis, Patrick, Liou, Kuo-Nan, and Yoshihide Takano (1993): Inference of Cirrus Cloud Properties Using Satellite-observed Visible and Infrared Radiances. Part I: Parameterization of Radiance Fields. *Journal of the Atmospheric Sciences*, **50**, p. 1279–1304.

[14] Piironen, P. and E. W. Eloranta (1993): Demonstration of an Iodine Absorption Filter Based High Spectral Resolution Lidar. Submitted to *Optics Letters*, on September 2, 1993.

[15] Platt, C. M. R. (1979): Remote Sounding of High Clouds: I. Calculation of Visible and Infrared Optical Properties from Lidar and Radiometer Measurements. *Journal of Applied Meteorology*, **18**, p. 1130–1143.

[16] Platt, C. M. R. and A. C. Dilley (1979): Remote Sounding of High Clouds: II. Emissivity of Cirrostratus. *Journal of Applied Meteorology*, **18**, p. 1144–1150.

[17] Platt, C. M. R.,Reynolds, David W., and N. L. Abshire (1980): Satellite and Lidar Observations of the Albedo, Emittance and Optical Depth of Cirrus Compared to Model Calculations. *Monthly Weather Review*, **108**, p. 195–204.

[18] Platt, C. M. R. (1981): The Effect of Cirrus of Varying Optical Depth on the Extraterrestrial Net Radiative Flux. *Quarterly Journal of the Royal Meteorological Society*, **107**, p. 671–678.

[19] Prabhakara, C., Fraser, R. S., Dalu, G., Wu, Man-Li C., Curran, R. J., and T. Styles (1988): Thin Cirrus Clouds: Seasonal Distribution Over Oceans Deduced from Nimbus–4 IRIS. *Journal of Applied Meteorology*, **27**, p. 379–399.

[20] Ramanathan, V., Pitcher, Eric J., and Maurice L. Blackmon (1983): The Response of a Spectral General Circulation Model to Refinements in Radiative Processes. *Journal of the Atmospheric Sciences*, **40**, p. 605–630.

[21] Sassen, Kenneth and Byung Sung Cho (1991): Subvisual–Thin Cirrus Lidar Dataset for Satellite Verification and Climatological Research. *Journal of Applied Meteorology*, **31**, p. 1275–1285.

[22] Shipley, S. T., Tracy, D. H., Eloranta, E. W., Trauger, J. T., Sroga, J. T., Roesler, F. L., and J. A. Weinman (1983): High Spectral Resolution Lidar to Measure Optical Properties of Atmospheric Aerosols. 1: Theory and Instrumentation. *Applied Optics*, **23**, p. 3716–3724.

[23] Smith, W. L. and C. M. R. Platt (1978): Comparison of Satellite-Deduced Cloud Heights with Indications from Radiosonde and Ground-Based Laser Measurements. *Journal of Applied Meteorology*, **17**, p. 1796–1802.

[24] Starr, David O'C. and Donald P. Wylie (1990): The 27–28 October 1986

FIRE Cirrus Case Study: Meteorology and Clouds. *Monthly Weather Review*, **118**, p. 2259–2287.

[25] Takano, Yoshihide and Kuo-Nan Liou (1989): Solar Radiative Transfer in Cirrus Clouds. Part I. Single–Scattering and Optical Properties of Hexagonal Ice Crystals. *Journal of the Atmospheric Sciences*, **46**, p. 3–19.

[26] Warren, S. G., Hahn, C. J., Chervin, R. M., and R. L. Jenne (1986): Global Distribution of Total Cloud Cover and Cloud Type Amounts over Land. NCAR Tech. Note NCAR/TN273+STR, [Available from National Center for Atmospheric Research, Boulder, CO 80307, NTIS DE87006903/XAB.] 228 pp.

[27] Woodbury, Gerard E., and M. P. McCormick (1986): Zonal and Geographical Distributions of Cirrus Clouds Determined by SAGE Data. *Journal of Geophysical Research*, **91**, p. 2775–2785.

[28] Wylie, D. P., and W. P. Menzel (1989): Two Years of Cloud Cover Statistics Using VAS. *Journal of Climate*, **2**, p. 380–392.

[29] Wylie, D. P., Menzel, W. P., Woolf, Harold M., and Kathy I. Strabala (1993): Four Years of Global Cirrus Cloud Statistics Using HIRS. Submitted to the *Journal of Climate* July 1993.